The complex dust formation zone of the AGB star IRC+10216 probed with CARMA 0.25 arcsec angular resolution molecular observations

J. P. Fonfría,[1]* M. Fernández-López,[2,3] M. Agúndez,[4] C. Sánchez-Contreras,[5] S. Curiel[6] and J. Cernicharo[4]

[1]*Departamento de Estrellas y Medio Interestelar, Instituto de Astronomía, Universidad Nacional Autónoma de México, Ciudad Universitaria, 04510 Mexico City, Mexico*
[2]*Instituto Argentino de Radioastronomía, CCT-La Plata (CONICET), C.C.5, 1894 Villa Elisa, Argentina*
[3]*Department of Astronomy, University of Illinois at Urbana-Champaign, 1002 West Green Street, Urbana, IL 61801, USA*
[4]*Laboratorio de Astrofísica Molecular, Departamento de Astrofísica, Centro de Astrobiología, INTA-CSIC, E-28850 Torrejón de Ardoz, Madrid, Spain*
[5]*Department of Astrophysics, Astrobiology Center (CSIC-INTA), Postal address: ESAC campus, PO Box 78, E-28691 Villanueva de la Cañada, Madrid, Spain*
[6]*Departamento de Astrofísica Teórica, Instituto de Astronomía, Universidad Nacional Autónoma de México, Ciudad Universitaria, 04510 Mexico City, Mexico*

ABSTRACT

We present low spectral resolution molecular interferometric observations at 1.2 mm obtained with the Combined Array for Research in Millimetre-wave Astronomy (CARMA) towards the C-rich AGB star IRC+10216. We have mapped the emission of several lines of SiS, $H^{13}CN$, SiO and SiC_2 in the ground and first excited vibrational states with a high angular resolution of 0.25 arcsec. These observations have allowed us to partially resolve the emission of the envelope at distances from the star $\lesssim 50$ stellar radii ($R_\star$), where the stellar wind is mainly accelerated. The structure of the molecular emission has been modelled with a 3D radiation transfer code. The emission of line SiS ($v = 0$, $J = 14$–13) is best reproduced with a set of maser emitting arcs arranged between 5 and $20 R_\star$. The abundance of $H^{13}CN$ with respect to H_2 decreases from 8×10^{-7} at 1–$5 R_\star$ to 3×10^{-7} at $20 R_\star$. The SiO observations are explained with an abundance $\lesssim 2 \times 10^{-8}$ in the shell-like region between 1 and $5 R_\star$. At this point, the SiO abundance sharply increases up to $(2$–3$) \times 10^{-7}$. The vibrational temperature of SiO increases by a factor of 2 due north-east between 20 and $50 R_\star$. SiC_2 is formed at the stellar surface with an abundance of 8×10^{-7} decreasing down to 8×10^{-8} at $20 R_\star$ probably due to depletion on to dust grains. Several asymmetries are found in the abundance distributions of $H^{13}CN$, SiO and SiC_2 which define three remarkable directions (north-east, south-southwest, and south-east) in the explored region of the envelope. There are some differences between the redshifted and blueshifted emissions of these molecules suggesting the existence of additional asymmetries in their abundance distributions along the line of sight.

Key words: masers – techniques: interferometric – stars: abundances – stars: AGB and post-AGB – circumstellar matter – stars: individual: IRC+10216.

1 INTRODUCTION

The asymptotic giant branch star (AGB) IRC+10216, considered the archetypical star of this type, has been extensively observed since its discovery (Becklin et al. 1969). Its C-rich circumstellar envelope (CSE) is mainly composed of dust and molecular gas. A large amount of molecules have been observed to date in this envelope (e.g. Kawaguchi et al. 1995; Cernicharo, Guélin & Kahane 2000; He et al. 2008). Among these molecules, just a few are formed close to the stellar photosphere (the so-called parent molecules such as C_2H_2, HCN, SiS, SiO, SiC_2 and CS; e.g. Keady & Ridgway 1993), while the rest arise in the outer shells, where the Galactic UV radiation is able to trigger a very active chemistry due to the small dust opacity.

The great sensitivity of the millimetre telescopes built in the last decades has been crucial to understand the chemistry in the outer envelope of IRC+10216. However, in spite of its proximity (123 ± 14 pc; Groenewegen et al. 2012), the small solid angle subtended by the innermost shells of its CSE has prevented from

*E-mail: fonfria@astro.unam.mx

achieving a deeper comprehension of the chemical evolution of the gas near the star, where even O-bearing molecules such as H_2O, typical in O-rich envelopes and previously believed to be marginally produced in C-rich ones, are observed with abundances larger than expected (Willacy & Cherchneff 1998; Melnick et al. 2001; Agúndez & Cernicharo 2006; Cherchneff 2006; Agúndez, Cernicharo & Guélin 2010; Decin et al. 2010a; Neufeld et al. 2011).

Previous works based on millimetre interferometric observations (Bieging & Tafalla 1993; Lucas et al. 1995; Monnier et al. 2000b; Young et al. 2004; Schöier et al. 2006b, 2007; Patel et al. 2009; Shinnaga et al. 2009), millimetre and submillimetre single-dish observations (Turner et al. 1987; Fonfría Expósito et al. 2006; Schöier, Olofsson & Lundgren 2006a; Cernicharo et al. 2010, 2011; Decin et al. 2010a,b; Agúndez et al. 2012), and infrared observations (Keady, Hall & Ridgway 1988; Keady & Ridgway 1993; Boyle et al. 1994; Schöier et al. 2006b; Fonfría et al. 2008) suggest that the abundance distributions of most of the parent molecules display essentially spherical symmetry. None the less, near-infrared continuum observations carried out with different techniques and high angular resolution (up to ∼1 mas; Ridgway & Keady 1988; Kastner & Weintraub 1994; Sloan & Egan 1995; Haniff & Buscher 1998; Weigelt et al. 1998; Richichi, Chandrasekar & Leinert 2003; Leão et al. 2006; Menut et al. 2007), indicate that the innermost dusty envelope displays a global bipolar morphology with its major axis roughly aligned along the NE–SW direction (PA $\simeq 20°$) and a size $\simeq 0.5 \times 0.3$ arcsec^2 (Men'shchikov et al. 2001; Men'shchikov, Hofmann & Weigelt 2002). The dusty envelope is also extremely clumpy and undergoes rapid time variations (Monnier, Geballe & Danchi 1998; Osterbart et al. 2000; Tuthill et al. 2000; Weigelt et al. 2002; Males et al. 2012). Hence, a complex chemical evolution of the gas linked to the dynamics of the inner layers of the CSE is expected (Willacy & Cherchneff 1998; Agúndez & Cernicharo 2006; Cherchneff 2006).

In this paper, we report new molecular observations at 1.2 mm towards IRC+10216 with angular resolutions as high as 0.25 arcsec. The observations were performed with the Combined Array for Research in Millimeter-wave Astronomy (CARMA)[1] and include several lines of SiS, H^{13}CN, SiO and SiC$_2$. In Section 2, we introduce the observations. The observational results derived from the analysis of the continuum and molecular emission are shown in Section 3. The observed molecular brightness distributions are fitted in Section 4. Section 5 contains the analysis of the fits, the comparison of the results with those of previous works, and a discussion of their implication. Finally, we present our main conclusions in Section 6.

1.1 The envelope of IRC+10216 and its molecular content

IRC+10216 is composed of a central variable star with a pulsation period $\simeq 625$–650 d (Witteborn et al. 1980; Ridgway & Keady 1988; Jones et al. 1990; Dyck et al. 1991; Le Bertre 1992; Jenness et al. 2002) and an angular radius, $\alpha_\star$, that ranges roughly between 15 and 25 mas along the pulsation (Ridgway & Keady 1988; Monnier et al. 2000a; Men'shchikov et al. 2001). Its local standard of rest (LSR) systemic velocity has been accurately estimated in -26.5 km s^{-1}

(e.g. Guélin, Lucas & Cernicharo 1993; Loup et al. 1993; He et al. 2008; Cernicharo et al. 2011). It is commonly accepted that the massive condensation of the refractory molecular species on to dust grains occurs in the so-called dust formation zone, which extends roughly from 5 up to about 20–50$R_\star$, where the terminal expansion velocity is reached ($\simeq 14.5$ km s^{-1}; e.g. Cernicharo et al. 2000; He et al. 2008). The expansion velocity field in this region of the CSE is not accurately determined and two different scenarios are usually adopted: (i) the gas is continuously accelerated from an expansion velocity of 2–3 km s^{-1} at $\simeq 5R_\star$, reaching the terminal velocity at 40–50$R_\star$ (e.g. Schöier et al. 2006b; Decin et al. 2010b), or (ii) the gas is mostly accelerated in two $\sim 1R_\star$ width shells located at $\simeq 5$ and 20$R_\star$ (inner and outer acceleration shells/zones, hereafter), where the expansion velocity is increased from 5 to 11 km s^{-1} and from 11 km s^{-1} to the terminal velocity, respectively. The line width is usually assumed to be $\simeq 5$ km s^{-1} at the stellar surface due to turbulence, decreases down to $\simeq 1$ km s^{-1} around the inner acceleration zone, and remains constant outwards (Keady et al. 1988; Keady & Ridgway 1993; Loup et al. 1993; Boyle et al. 1994; Fonfría et al. 2008; Cernicharo et al. 2011; Agúndez et al. 2012). Other scenarios are also possible, such as an irregular gas expansion velocity field linked to dust clumps moving close to the star (e.g. Menut et al. 2007).

SiS is one of the most abundant species in the innermost envelope of IRC+10216 (Keady & Ridgway 1993; Boyle et al. 1994; Agúndez et al. 2012, Fonfría et al., in preparation). The drop observed in its abundance profile across the dust formation zone is usually attributed to the refractory nature of this Si-bearing molecule, which would favour its deposition on to the dust grains (Boyle et al. 1994; Decin et al. 2010b; Agúndez et al. 2012). At scales larger than 5 arcsec, the brightness distribution is roughly spherical (Bieging & Nguyen-Quang-Rieu 1989; Bieging & Tafalla 1993), while higher angular resolution observations [Half-power beamwidth (HPBW) $\simeq 3$ arcsec] reveal an elongation along the direction with a PA $\simeq 20°$ (Lucas et al. 1995). Maser emission has been detected in several rotational lines coming from the dust formation zone (Henkel, Matthews & Morris 1983; Carlström et al. 1990; Fonfría Expósito et al. 2006). One of them, SiS ($v = 0$, $J = 14$–13), is analysed in the current work.

H^{13}CN is probably formed at the stellar photosphere, where emission of very high excitation ro-vibrational levels of HCN have been observed (Cernicharo et al. 2011) and thermodynamical equilibrium (TE) is supposed to prevail (e.g. Willacy & Cherchneff 1998; Agúndez & Cernicharo 2006). The abundance profile derived from single-dish and interferometric observations displays a somewhat complex dependence on the distance to the star before $\simeq 20$–50$R_\star$ from where the abundance remains nearly constant (Schöier et al. 2007; Fonfría et al. 2008; Shinnaga et al. 2009).

SiO seems to be formed near the star as well (Willacy & Cherchneff 1998; Agúndez & Cernicharo 2006). The abundance distribution in the inner shells of the envelope is still a controversial topic since some works derived constant abundances (Keady & Ridgway 1993; Schöier et al. 2006a; Agúndez et al. 2012) while others found more complex distributions in which there is a significant increase of the abundance at distances to the star $\lesssim 8R_\star$ (Schöier et al. 2006b; Decin et al. 2010b). All the observations carried out to date (HPBW $\gtrsim 2$ arcsec) are compatible with a roughly spherical abundance distribution.

The emission of SiC$_2$ is composed of a bright compact region surrounding the central star and a detached and clumpy shell with a radius of about 15 arcsec, which is apparently hollow and displays a marked bipolar emission along the NE–SW direction

Table 1. Summary of observations at 257 GHz towards IRC+10216.

Epoch	Configuration	Baselines	Time[a]	τ_{230}	Phase calibrator flux[b]	Synthesized Beam[c]		rms[c]
						HPBW	PA	
		(m)	(h)		(Jy)	(arcsec^2)	($^\circ$)	(mJy beam^{-1})
2011 Jan 5	B	60–800	3.1	0.07	3.8	0.3×0.2	57	10
2012 Mar 8	C	20–300	3.9	0.12	3.4	0.7×0.6	89	10

Note: [a]On source integration time after removal of bad weather periods.
[b]Flux set to the phase calibrator 0854+201. It was estimated from the CARMA and the SMA quasar monitoring.
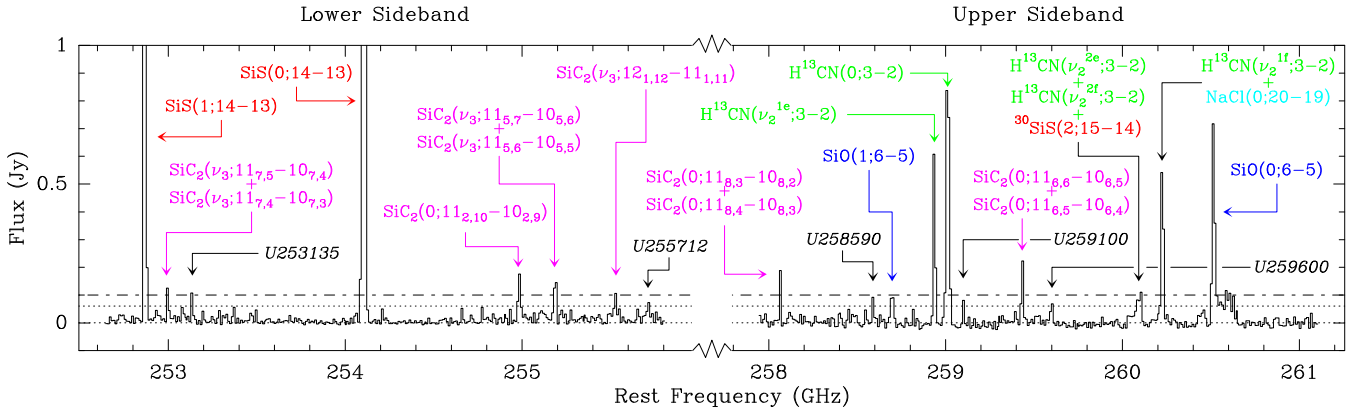[c]Estimated from the continuum images.

Figure 1. Observed spectrum of IRC+10216 in B configuration. It contains lines of SiS (red), H^{13}CN (green), SiO (blue), SiC$_2$ (magenta) and several unidentified features (black). The lower dotted line indicates the baseline after the continuum removal, the upper one indicates the 3σ level and the dash–dotted line corresponds to the 5σ level. The rms of the noise ($\sigma \simeq 20$ mJy) has been estimated from frequency ranges where the spectrum is apparently free of lines. The molecular transitions associated to the observed lines are labelled with the vibrational state in which they are produced (within the parentheses, to the left) and the rotational quantum numbers of lower and upper levels, $J_{up} - J_{low}$ (within the parentheses, to the right). The overlaps between lines have been designated by means of the symbol +. The unidentified lines have been denoted in the usual way.

(Takano, Shaito & Shuji 1992; Gensheimer, Likkel & Snyder 1995; Lucas et al. 1995; Cernicharo et al. 2010). This brightness distribution suggests that SiC$_2$ is formed near the star, gets depleted in the dust formation zone, and again reappears in the outer CSE probably due to the action of the Galactic UV radiation field on the expanding matter.

2 OBSERVATIONS

The observations analysed in this work were carried out on 2011 January 5 and 2012 March 8 with the CARMA interferometer (Table 1). The array was used in its 15-antenna mode. It comprised six 10.4 m and nine 6.1 m antennas that were arranged in B and C configurations, with baselines in the ranges 70–800 and 20–300 kλ and system temperatures of about 200 and 500 K, respectively. The weather was good during both observing runs, with an atmospheric opacity $\simeq 0.1$ at 230 GHz.

The correlator setup included 16 spectral windows (8 windows per sideband symmetrically distributed from the first local oscillator frequency), each with a configurable band width. The frequency of the first local oscillator was tuned at $\simeq 257$ GHz. In B configuration, the correlator setup included 14 spectral windows of 500 MHz and a spectral resolution of 10.4 MHz ($\simeq 12.0$–12.3 km s^{-1} at the observed frequency). These wide bands covered the line emission from several molecular species (Fig. 1, Table 2). In C configuration, four 500 MHz bands were included and the main lines detected in B configuration were covered with narrower 62 MHz bands (spectral resolution of 0.2 km s^{-1} at the observed frequency). To combine the data from both configurations we binned the C configuration data

into 12.3 km s^{-1} channels. The high spectral resolution observations will be presented elsewhere.

The calibration and data reduction were performed in the standard way using the MIRIAD package. Bandpass solutions were obtained observing 3C84, while 0854+201 was periodically observed to calibrate phases. Calibrator 0854+201 was assumed to have flux densities of 3.8 and 3.4 Jy at 257 GHz in 2011 January and 2012 March, respectively, as determined by the CARMA and Submillimeter Array quasar monitoring programmes near the time of our observations. The absolute flux calibration uncertainty is about 15 per cent.

The phase centre displayed an offset between B and C configuration observations. In order to combine the data from both configurations at the inverse Fourier transform step, we shifted the coordinates of the phase centre of the data from C configuration using the MIRIAD task UVEDIT. We applied a natural weighting to all data sets and obtained B, C, and combined BC maps of IRC+10216. Maps obtained from B configuration data have a synthesized beam of about 0.25 arcsec, while those obtained from C configuration data have a synthesized beam of 0.7 arcsec. Combined maps resulted in intermediate resolutions (HPBW $\simeq 0.38$–0.46 arcsec) depending on the robust parameter (Briggs 1995; Briggs, Schwab & Sramek 1999). This parameter weights the data according to the number of visibilities measured in each *uv* space cell. In MIRIAD, the parameter robust $\gtrsim 2$ and $\lesssim -1$ corresponds to natural and uniform weighting, respectively. The natural weighting produces maps with lower rms noise level while the uniform weighting provides better angular resolution at the expense of increasing sidelobe levels. Values between these limits give a compromise between both. The primary

Table 2. Parameters of observed lines in B configuration.

Molecule	Transition		ν_{rest}	E_{up}/k	V_{LSR}	FWHM	Peak flux	Integrated flux
	Vib. State	J_{up}–J_{low}	(MHz)	(K)	(km s^{-1})	(km s^{-1})	(Jy)	(Jy km s^{-1})
Identified lines								
SiS	$v=0$	14–13	254 103.2108	91.5	-25 ± 6	18 ± 6	13.12 ± 0.02	250 ± 80
	$v=1$	14–13	252 866.4683	1162.2	-27 ± 6	17 ± 6	2.25 ± 0.02	40 ± 15
^{30}SiS	$v=2$	15–14	260 074.7218^a	2196.9	-31 ± 6	6 ± 6	0.24 ± 0.02	1.5 ± 1.7
H^{13}CN	$v=0$	3–2	259 011.7978	24.9	-26 ± 6	21 ± 6	1.01 ± 0.02	23 ± 7
	ν_2^{1e}	3–2	258 936.0502	1040.6	-27 ± 6	14 ± 6	0.70 ± 0.02	10 ± 5
	ν_2^{1f}	3–2	260 224.8132	1040.7	-26 ± 6	18 ± 6	0.62 ± 0.02	12 ± 4
	$2\nu_2^{2e}$	3–2	260 094.0$^{\star a}$	2964*	-32 ± 6	6 ± 6	0.16 ± 0.02	1.0 ± 1.2
	$2\nu_2^{2f}$	3–2	260 104.2$^{\star a}$	2964*	-32 ± 6	6 ± 6	0.16 ± 0.02	1.0 ± 1.2
SiO	$v=0$	6–5	260 518.0200	43.8	-24 ± 6	18 ± 6	0.73 ± 0.02	14 ± 5
	$v=1$	6–5	258 707.3900	1812.6	-28 ± 6	26 ± 6	0.10 ± 0.02	2.8 ± 1.2
SiC$_2$	$v=0$	$11_{2,10}$–$10_{2,9}$	254 981.4940	81.9	-29 ± 6	20 ± 6	0.17 ± 0.02	3.6 ± 1.5
	$v=0$	$11_{8,3}$–$10_{8,2}$	258 065.0545^b	199.4	-23 ± 6	9 ± 6	0.26 ± 0.02	2.5 ± 1.8
	$v=0$	$11_{8,4}$–$10_{8,3}$	258 065.0545^b	199.4				
	$v=0$	$11_{6,6}$–$10_{6,5}$	259 433.3090^c	144.9	-27 ± 6	14 ± 6	0.23 ± 0.02	3.4 ± 1.8
	$v=0$	$11_{6,5}$–$10_{6,4}$	259 433.3090^c	144.9				
	ν_3	$11_{7,5}$–$10_{7,4}$	252 998.2722^d	454.8	-27 ± 6	10 ± 6	0.18 ± 0.02	1.9 ± 1.4
	ν_3	$11_{7,4}$–$10_{7,3}$	252 998.2743^d	454.8				
	ν_3	$11_{5,7}$–$10_{5,6}$	255 180.2915^e	406.5	-28 ± 6	17 ± 6	0.16 ± 0.02	2.9 ± 1.4
	ν_3	$11_{5,6}$–$10_{5,5}$	255 191.7263^e	406.5				
	ν_3	$12_{1,12}$–$11_{1,11}$	255 525.3490	365.1	-28 ± 6	18 ± 6	0.10 ± 0.02	1.9 ± 1.0
Unidentified lines								
U253135			253 135			12 ± 6	0.10 ± 0.02	1.3 ± 0.9
U255712			255 712			28 ± 6	0.06 ± 0.02	1.8 ± 1.0
U258590			258 590			10 ± 6	0.12 ± 0.02	1.3 ± 1.0
U259100			259 100			14 ± 6	0.10 ± 0.02	1.5 ± 0.9
U259600			259 600			18 ± 6	0.08 ± 0.02	1.5 ± 0.9

Most of the rest frequencies and the energies of the upper levels of the transitions have been taken from the CDMS Catalogue (Müller et al. 2005; http://www.astro.uni-koeln.de/cdms/catalog). Those marked with symbol * have been adopted from Cernicharo et al. (2011). We have performed Gaussian fits to the lines with the aid of the GreG package included in GILDAS. From these fits, we have retrieved the velocity of the peak flux (V_{LSR}), the line width of the observed lines (FWHM), the peak flux (Peak flux), and the area of the observed lines (Integrated flux). The uncertainties of magnitudes V_{LSR} and FWHM have been assumed to be the half of a channel ($\simeq 6$ km s^{-1}). We have adopted the rms of the spectrum as the error of the peak emission ($\simeq 20$ mJy). The uncertainties of the flux density has been calculated from the latter errors. The lines whose frequencies go with the same letter (a, b, c, ...) are blended. The parameters of the blended lines have been estimated during the fitting procedure by assuming the lines have similar emissions.

beam of the observations was 30 arcsec for both configurations. The imaging and analysis of the data were done using the packages MIRIAD and GILDAS.

In this work, we present and analyse the line-free continuum data and the spectral data from five molecular lines observed in both B and C configurations: SiS($v = 0$, $J = 14$–13), H^{13}CN($v = 0$, $J = 3$–2), SiO($v = 0$, $J = 6$–5), SiO($v = 1$, $J = 6$–5) and SiC$_2$ ($v = 0$, $J_{K_a,K_b} = 11_{2,10} - 10_{2,9}$).

2.1 Extended emission

It could be argued that the lack of short baselines in our observations would critically affect the derived maps invalidating our results. In fact, the absence of these baselines prevents us from detecting emission coming from structures with large characteristic lengths which could be significant. If we adopt a Gaussian to roughly represent the smallest structure missed by C configuration, it would be described by a full width at half-maximum (FWHM) in the uv plane of $\simeq 50$ kλ. This Gaussian would have an FWHM in the image plane of about 4 arcsec in average [FWHM$_{\text{image plane}}$(arcsec) $\simeq 182$/FWHM$_{uv\,\text{plane}}$(kλ)]. The lack of such structure in our observations compared with other observations with a better coverage of

the uv plane close to its origin would be reflected in (i) a smaller emission coming from the surroundings of the star, and (ii) a significantly lesser flux density in the regions of the brightness distribution at distances from the star $\gtrsim 2$ arcsec. However, the small features in the emission would not be modified since that Gaussian structure would not have a meaningful contribution to the visibility at long baselines. Hence, since we are interested in the shape of the observed distributions closer to the star than 1 arcsec, the lack of short baselines is not an issue and we do not expect serious modifications with respect to the actual brightness distributions.

3 OBSERVATIONAL RESULTS

3.1 Continuum emission

The brightness distribution of the continuum of IRC+10216 at 257 GHz is compatible with a point source in B and C configurations. The integrated flux density is $\simeq 0.38$, and 0.53 Jy for the maps in B and C configurations, respectively, with an uncertainty of 15 per cent. Some unresolved observations of the source at different frequencies with similar point spread functions (PSFs) to that of our C configuration observations can be found in the literature;

Lucas & Guélin (1999) reported the fluxes ≃0.32, 0.41 and 0.49 Jy at 216, 235 and 242 GHz, respectively, with the Plateau de Bure Interferometer (PdBI) and an HPBW ≃0.5 arcsec, Lucas (1997) derived a flux ≃0.48 Jy at 233 GHz also with the PdBI and an HPBW ≃0.75 arcsec, and Patel et al. (2009) obtained 0.84 and 1.17 Jy at 301.1 and 337.5 GHz, respectively, with the SMA and an HPBW ≃ 0.7 arcsec. All these data can be used to estimate the spectral index of the spectral energy distribution of IRC+10216. The pulsation phase during our observations was 0.5 (Jenness et al. 2002), while it was ≃0.2 and 0.3 when the observations by Patel et al. (2009) and Lucas (1997) happened. Lucas & Guélin (1999) did not indicate the date of their observations. After correcting the fluxes from the different phase with the aid of the time dependent emission formula at 850μm proposed by Jenness et al. (2002), we derive a spectral index ≃2.53 ± 0.15. The uncertainties in the flux calibration rises this error to 0.7. Thus, this spectral index is compatible with that of a blackbody (Young et al. 2004; Menten et al. 2006).

3.1.1 Source position and proper motions

The position of the continuum source (which we will assume the same as that of the central star, hereafter) can be determined after calibration by fitting a Gaussian to the flux density distribution. From the B configuration data, we found that the star is at α(J2000) = $09^h47^m57\overset{s}{.}435 \pm 0.002$ s and δ(J2000) = $13°16'43\overset{''}{.}86 \pm 0\overset{''}{.}03$, in good agreement with the results previously reported by Patel et al. (2009). The uncertainty of this position has been estimated by adding the statistical and systematic uncertainties in quadrature (see e.g. Downes et al. 1999; Maness et al. 2008). The former is

$$\Delta\theta \simeq \left(\frac{4}{\pi}\right)^{1/4} (8\ln 2)^{1/2} \frac{\theta_{beam}}{SNR} \quad , \tag{1}$$

where θ_{beam} is the HPBW of the synthesized beam and SNR is the signal-to-noise ratio of the observed source. In our case, the statistical error is $0\overset{''}{.}01$. Regarding the systematic positional uncertainty, we have used two independent methods to estimate it. In the first one, we measure the position of the peak emission of IRC+10216 in each observing cycle, after the data had been calibrated with 0854+201 but before self-calibration, to avoid information losses on the position of the source (e.g. Menten et al. 2006). In the second method, we determine the rms of the visibility phases of the calibrator 0854+201 for baselines longer than 200 m, which provide the positional accuracy for the most compact sources, such as IRC+10216. Both methods agree quite well resulting in a positional error due to systematics of $0\overset{''}{.}03$. The total positional uncertainty for the continuum source is thus ≃$0\overset{''}{.}03$.

This peak position is accurate enough to derive the proper motions of the continuum source of IRC+10216 comparing it with the measurements published previously in the literature. We have used the continuum position and the uncertainties obtained by Drake et al. (1991) and Menten et al. (2006), which are based on centimetre observations (1.3, 2, 3.5 and 6 cm) carried out with the Very Large Array (some of them in the A configuration) between years 1987 and 1993. In order to estimate the proper motions, we have assumed that the continuum peak emission in the cm and mm wavelength ranges is produced at the same place. The proper motions of IRC+10216 derived in the frame of this work are (μ_α, μ_δ) = (34 ± 4, 12 ± 4) mas yr^{-1}, in good agreement with (26 ± 6, 4 ± 6) mas yr^{-1} derived by Menten et al. (2006) and, particularly, with (35 ± 1, 12 ± 1) mas yr^{-1}, recently proposed by Menten et al. (2012).
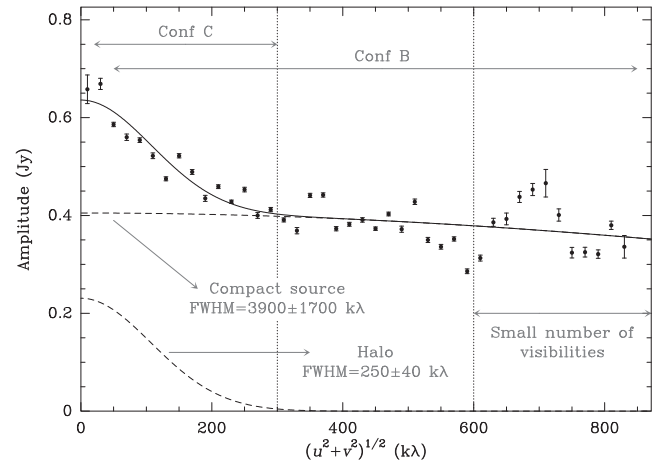

Figure 2. Amplitude of the visibility for the continuum emission as a function of the uv-distance. The amplitude has been averaged out in rings of 20 kλ width with the MIRIAD routine UVAMP. Error bars give the typical deviation of the amplitude for each ring. The data can be fitted with two Gaussians (dashed black curves). Their sum has been plotted as the solid black curve.

3.1.2 Structure of the continuum source

In Fig. 2, we have plotted the amplitude of the visibility as a function of the uv-distance. A simple inspection leads to the identification of two different regimes below and over ≃200–250 kλ, where the gradient of the amplitude changes significantly. The data set can be fitted with two Gaussians centred in the origin of the uv plane. Their FWHMs are 250 ± 40 and 3900 ± 1700 kλ, i.e. 0.73 ± 0.12 and 0.05 ± 0.02 arcsec in the image plane, respectively. The average amplitudes over 600 kλ are noisier than the rest of the data set probably as a consequence of the scarcity of long baselines in B configuration. Therefore, to first order, the continuum emission comes from a compact source embedded in a halo.

3.2 Molecular emission

The correlator setup allowed for the simultaneous detection of several molecular lines through a band width coverage of ≃6.4 GHz. The spectrum of both sidebands can be seen in Fig. 1. We have found 25 molecular lines over the 3σ detection level. Twenty of them have been identified. Four unidentified lines have also been detected in the molecular survey ranging from 255.3 to 274.8 GHz carried out with Atacama Large Millimeter Array and partially presented by Cernicharo et al. (2013). Table 2 contains their frequencies and the parameters derived from a Gaussian-line fitting procedure. Those 20 identified lines have been observed in B configuration and 5 of them also in C configuration.

Fig. 3 shows the moment 0 maps of some of the identified lines in B and the jointly combined BC configurations calculated with natural weighting (robust=2). The observed distributions are roughly fitted with one or two elliptical Gaussians using the MIRIAD routine IMFIT. We have assumed as reasonable fits those with less than 3σ residuals at any position inside the fitting region. Table 3 contains a summary of these fits. In Fig. 4, we have plotted the redshifted and blueshifted emission of the H^{13}CN and SiO lines in the vibrational ground state.

In order to compare the flux measurements in B and C configurations for the lines observed in both, we have determined the average flux density for each configuration in the region of the uv plane
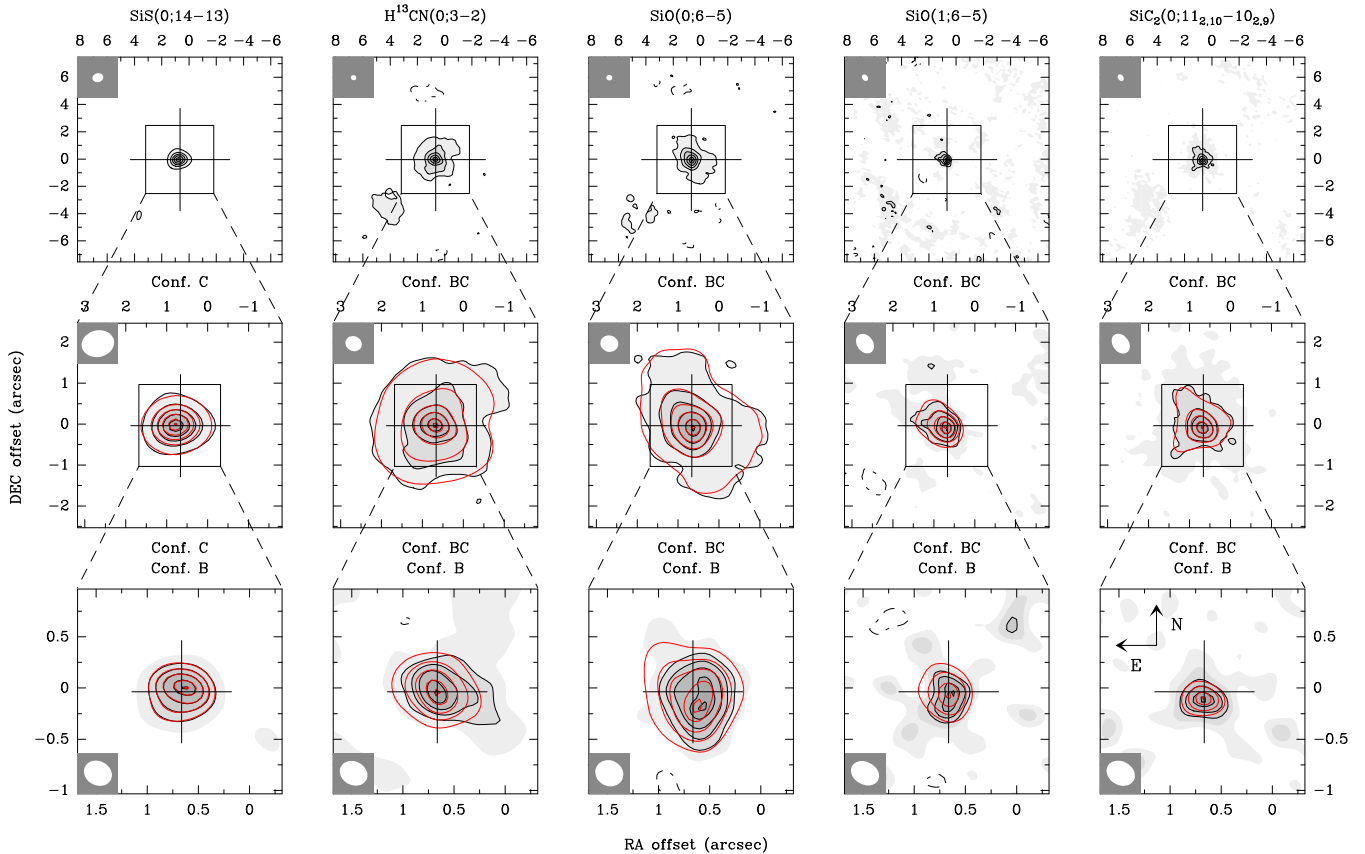
Figure 3. Moment 0 maps of the most intense observed lines: SiS($v = 0$, $J = 14$–13), H^{13}CN($v = 0$, $J = 3$–2), SiO($v = 0$, $J = 6$–5), SiO($v = 1$, $J = 6$–5) and SiC$_2$($v = 0$, $J_{K_a K_b} = 11_{2,10} - 10_{2,9}$). The top and middle rows show the maps for BC configuration (except for the SiS line) while the bottom row includes the maps of the observations in B configuration. In the case of SiS($v = 0$, $J = 14$–13), the map in C configuration has been included instead that in BC configuration because of an incompatibility detected between the observations in B and C configurations (see Sections 3.2 and 5.2, and Table 4). Each column contains the brightness distributions of a single line. All the distributions have been mapped with natural weighting (`robust=2`). The coordinates in the maps are the offsets with respect to the centre of phases located at α(J2000) = 09^{h}47^{m}57^{s}39 and δ(J2000) = +13°16′43″90. The black crosses indicate the position of the star (Section 3.1.1). The positive contours for each insert are at levels 10, 30, 50, 70, 90 and 99 per cent of the peak emission. The highest levels are always present. The minimum level depends on the map. The only plotted negative contour is at a level equal to the opposite of the lowest positive contour. See Table 3 for the peak emissions. The red contours in the middle and lower rows are the fits to the observed maps performed with our code (see Section 4).

where the set of uv distances for both configurations overlap (200–300 kλ). The C/B ratio between fluxes from C and B configuration ranges from 0.8 to 1.5 for most of them (see Table 4). However, this ratio raises to $\simeq$9 for line SiS($v = 0$, $J = 14$–13). This variation is not due to uncertainties in the flux calibration and, therefore, represents an actual evolution of the line emission (see Section 5.2).

3.2.1 SiS

The brightness distributions of line SiS($v = 0$, $J = 14$–13) in C and B configurations show circular symmetry (Fig. 3). Their sizes are smaller than expected for a line supposed to display extended emission. The peak emission is located roughly on the star in the naturally weighted maps although an offset due NW might exist (Table 3). However, it is offset with respect to the star by $\simeq$70 ± 40 mas due NW in the uniformly weighted (`robust=-1`) B configuration map (not shown; HPBW = 0.27 × 0.20 arcsec^2, PA = 87°). The emission in this map is barely resolved and required a two-Gaussian fit. These two Gaussians are centred at the peak emission and at the SE of the star position. The blue–red factor, defined as

the ratio of the flux densities from the blueshifted and redshifted emission, is 1.2 and 1.0 in the naturally weighted maps in the C and B configurations, respectively (see Table 3).

The emission of the vibrationally excited line SiS($v = 1$, $J = 14$–13, not shown) is characteristic of a compact source centred at the star position. Its blue–red factor is 1.2.

3.2.2 H^{13}CN

The brightness distribution of line H^{13}CN($v = 0$, $J = 3$–2) in BC configuration shows an overall extended emission more prominent along the N–S direction at 2 arcsec scale (Fig. 3). At smaller scales ($\simeq$1 arcsec), there is a possible E–W elongation in the surroundings of the star. This is reflected in the two-Gaussian fit we carried out to the emission. Fig. 4 shows that the redshifted emission in B configuration mapped with natural weight peaks at the star position while the blueshifted emission displays an elongation roughly along the NE–SW direction. The uniformly weighted map in B configuration suggests that this elongation is composed of two clumps, one to the N-NE of the star and the other to the S-SW.

Table 3. Characterization of the moment 0 maps of the most intense lines with natural weighting (`robust=2`).

Line	Conf.	Observations F_{int} (Jy km s^{-1})	F_{max} (Jy beam^{-1} km s^{-1})	Peak (mas)	Gaussian fit Centre (mas)	Size (arcsec^2)	PA (°)	PSF Size (arcsec^2)	PA (°)	BR
SiS(0; 14–13)	C	1710 ± 140	1200 ± 25	(90, 30)	(78, 1)	0.97 × 0.79	−85	0.80 × 0.65	−78	1.2
	B	740 ± 70	200 ± 8	(−30, 30)	(−18, 0)	0.58 × 0.48	80	0.28 × 0.24	62	1.0
SiS(1; 14–13)	B	54 ± 4	33.6 ± 0.8	(0, −20)	(−12, −11)	0.35 × 0.31	47	0.28 × 0.23	50	1.2
H^{13}CN(0; 3–2)	BC	600 ± 90	50.1 ± 2.3	(30, 30)	(10, 10)	0.71 × 0.54	70	0.41 × 0.36	65	0.8
					(29, 20)	2.37 × 1.97	−30			
	B	47 ± 9	13.0 ± 1.3	(−15, −20)	(−98, 5)	0.78 × 0.51	70	0.28 × 0.23	63	1.1
H^{13}CN(ν_2^{1e}; 3–2)	B	13.1 ± 2.0	9.0 ± 0.7	(−15, −20)	(−22, −11)	0.36 × 0.34	49	0.28 × 0.23	63	0.8
H^{13}CN(ν_2^{1f}; 3–2)	B	13.7 ± 1.7	10.6 ± 0.5	(−45, −20)	(−26, −12)	0.35 × 0.29	73	0.28 × 0.23	58	0.9
SiO(0; 6–5)	BC	390 ± 60	44.7 ± 1.8	(−60, −50)	(22, −19)	1.02 × 0.85	29	0.44 × 0.40	75	0.7
					(−78, 174)	3.31 × 2.28	39			
	B	52 ± 7	11.4 ± 0.9	(−135, −170)	(−76, −64)	0.69 × 0.53	10	0.28 × 0.25	63	0.6
SiO(1; 6–5)	BC	10.1 ± 2.1	5.2 ± 0.6	(−15, −50)	(137, −4)	0.99 × 0.70	52	0.52 × 0.39	37	0.5
	B	4.0 ± 1.0	2.6 ± 0.5	(−75, −10)	(−11, −63)	0.49 × 0.36	−13	0.29 × 0.22	61	–
SiC$_2$(0; 11$_{2, 10}$–10$_{2, 9}$)	BC	31.3 ± 2.2	6.7 ± 0.5	(0, −50)	(−9, −52)	0.57 × 0.49	50	0.53 × 0.39	36	1.1
					(114, 102)	2.10 × 1.94	−6			
	B	4.6 ± 1.1	3.1 ± 0.5	(−15, −60)	(−7, −83)	0.44 × 0.38	70	0.29 × 0.23	61	1.2
SiC$_2$(ν_3; 11$_{5, 7}$–10$_{5, 6}$) + SiC$_2$(ν_3; 11$_{5, 6}$–10$_{5, 5}$)	B	2.9 ± 0.8	2.9 ± 0.5	(−15, −20)	(1, 8)	0.37 × 0.35	−57	0.29 × 0.23	61	1.2

From left to right, the columns contain the label of each molecular line, the CARMA configuration (B, BC, or C), the integrated flux density over the 3σ level, the integrated peak emission and its position with respect to the star (RA and Dec.), the centre of the Gaussian used in the fit with respect to the star (RA and Dec.), its FWHM and position angle, the HPBW and position angle of the PSF, and the blue–red factor defined as the ratio of the flux density of the blueshifted emission to that of the redshifted one with respect to the systemic LSR velocity. The observed distributions have been fitted adopting one or two Gaussians with the routine IMFIT. We have assumed as reasonable fits those for which the fitting function departs from the distribution in less than 3σ. When the fit to the observed brightness distribution must be performed with two Gaussians, the parameters of the second Gaussian are arranged in the following line. All the positions are expressed as offsets with respect to the position of the central star (Section 3.1.1). The uncertainties of most of the axis of the Gaussians are smaller than 10 per cent although they reach 30 per cent in few cases. The uncertainty of the position angles is usually smaller than 10°. The blue–red factor of line SiO($v = 1$, $J = 6$–5) in B configuration cannot be estimated because the blueshifted emission is too weak.

The vibrationally excited lines H^{13}CN(ν_2^{1e}, $J = 3$−2) and H^{13}CN(ν_2^{1f}, $J = 3$−2, not shown) display a compact point-like brightness distribution centred at the star.

3.2.3 SiO

Fig. 3 shows the SiO($v = 0$, $J = 6$–5) emission mainly extended and with an overall preferred NE–SW direction at 3 arcsec scales. At these scales, the blueshifted emission is preferentially seen towards the NE, while the redshifted emission is elongated towards the SW, evidencing a possible bipolar outflow along this direction, although with a severe overlap between the redshifted and blueshifted emission towards the central region (Fig. 4).

The peak emission of the distribution of line SiO($v = 0$, $J = 6$–5) in the high angular resolution maps (with a $\simeq 0.25$ arcsec beam) is shifted to the SW. The redshifted emission is single peaked while the blueshifted emission shows multiple peaks forming an arc-like feature surrounding the position of the redshifted peak.

In good agreement with the other vibrationally excited molecular transitions, SiO($v = 1$, $J = 6$–5) is a compact source peaking at the 5σ level. A Gaussian fit to its BC configuration emission gives a somewhat elongated source with a PA $\simeq 50°$.

3.2.4 SiC$_2$

The SiC$_2$($v = 0$, $J_{K_a K_b} = 11_{2,10} - 10_{2,9}$) emission is mostly circular at scales of 1 arcsec but it seems to be elongated along the NE and SE directions at scales of 2 arcsec.

The emission of the vibrationally excited lines in B configuration (not shown) is compact and centred on the star position.

4 FITTING THE MOLECULAR EMISSION

The observations presented in Section 3.2 evidence the existence of structure in the emission of each molecular line not mapped to date. Deviations from spherical symmetry could be due to particular features or global asymmetries either in the abundance with respect to H$_2$ and/or excitation temperature distributions of each molecule, or in magnitudes describing the gas component of the envelope as the H$_2$ density and/or the expansion velocity field. Other structures such as sets of clumps have not been considered since these clumps would be substantially smaller than the PSF of our observations and their effect could not be distinguished from that of an equivalent continuous structure. In order to describe the molecular content of the dust formation zone in IRC+10216, we have explored the spatial dependence of the abundance with respect to H$_2$ and the vibrational temperature for each molecule. The analysis of the magnitudes that describe the gas (H$_2$ density, expansion velocity) has been done after fitting the molecular observations by looking for shared features or asymmetries in all the abundance distributions.

The fits to the emission of the molecular lines have been performed with an improved 3D version of the 1D radiation transfer code developed by Fonfría et al. (2008), which numerically solves the radiation transfer equation in a spherically symmetric circumstellar envelope composed of molecular gas and dust. The new version of the code is able to deal with diatomic, linear and symmetric top molecules in addition to asymmetric top molecules after diagonalizing the Watson's Hamiltonian in its A-reduction I^r representation, suitable for the case of SiC$_2$ (Fonfría et al. 2008, 2011; Müller et al. 2012). The statistical equilibrium equations (SE) *are not solved*. The populations of the molecular levels are computed from the rotational and vibrational temperature distributions that are
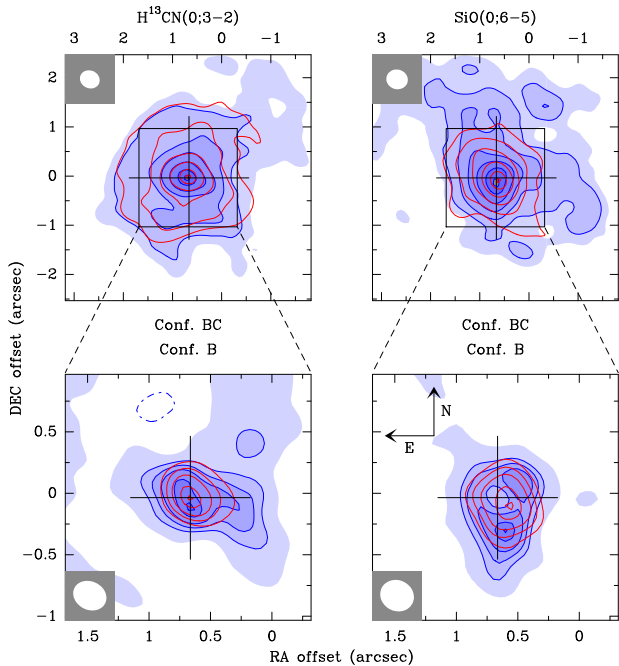
Figure 4. Redshifted and blueshifted emission (in red contours and blue contours and colour scale, respectively) of lines $H^{13}CN$ ($v = 0$, $J = 3–2$) and SiO ($v = 0$, $J = 6–5$) in BC (upper inserts) and B (lower inserts) configurations. All the emissions have been mapped assuming natural weighting (robust=2). The contours in the maps in BC configuration are at levels -15, 15, 30, 50, 70, 90 and 99 per cent of the peak emission. They are at -40, 40, 55, 70, 90 and 99 per cent of the peak emission for maps in B configuration. The colour scale in the lower right insert reveals an emission deficit around the star in the blueshifted emission map.

Table 4. Flux density in the overlap region of the *uv* plane.

Source	Conf. B	Conf. C	Factor C/B
Continuum	405 ± 5	389 ± 3	1.0
$H^{13}CN(0; 3 - 2)$	470 ± 4	724 ± 20	1.5
SiO(0; 6 - 5)	466 ± 5	565 ± 20	1.2
SiO(1; 6 - 5)	421 ± 5	383 ± 20	0.9
$SiC_2(0; 11_{2, 10} - 10_{2, 9})$	401 ± 5	309 ± 20	0.8
SiS(0; 14 - 13)	925 ± 4	8100 ± 40	8.8

The first column contains the source (molecular line or continuum). The second and third columns account for the average amplitudes expressed in mJy in the overlap region of the *uv* plane derived from the observations in B and C configurations. The fourth column is devoted to the ratio of the amplitudes in C configuration to B in the overlap range. Most of the ratios depart from 1 in no more than $\simeq 50$ per cent, typical for compatible observations of different configurations. The ratio for line SiS($v = 0$, $J = 14–13$) is much larger suggesting an unavoidable incompatibility between the observations in B and C configurations.

input data as well as the molecular abundance with respect to H_2, the H_2 density profile, and the expansion and turbulence velocity fields (see Section A2 of Appendix A for a deeper description of the program). Our code can also reproduce maser emission assuming a negative excitation temperature in the maser emitting region to get the required population inversion. The contribution of the maser emitting volumes to the total synthetic emission is calculated in the same way and with the same mathematical expressions than for the thermal emitting volumes. Thus, the velocity coherence has

been taken into account and the code derives the exact solutions for the maser emission within the typical uncertainty $\lesssim 1$ per cent. This code was developed to solve the radiation transfer equation for any gas expansion velocity field adopted, allowing us to derive the emission of any region of an asymmetric CSE. Thus, it is particularly useful to analyse the innermost envelope of IRC+10216, where the velocity gradient is similar to the line widths.

The code allows any molecular abundance with respect to H_2 and rotational and vibrational temperature distributions expressed in spherical coordinates. We identify the z-axis of the reference system with the line-of-sight (LoS). The polar angle, θ, is measured from behind the star towards the Earth and the axial angle (or position angle), φ, from N to E. The code calculates the emission for several axial angles and performs a linear interpolation on φ for any other axial angle (see Section A1 of Appendix A for a description of the gridding and sampling of the physical and chemical magnitudes). A realistic coverage of the uv plane has been achieved by replacing the calibrated visibilities in the MIRIAD data files with those of the synthetic emission using the MIRIAD's routine UVMODEL. This method applies on the synthetic emission the same constraints imposed by the array configuration on the actual brightness distribution.

The performance of our code was tested in 1D against (i) simple scenarios, whose solutions have been calculated analytically or numerically through independent ad hoc codes, and (ii) the non-local, non-LTE radiation transfer code developed by Daniel & Cernicharo (2008) for static and expanding envelopes which emits optically thin and thick lines produced under local thermodynamic equilibrium (LTE), with positive excitation temperatures depending on the distance to the star, or with negative excitation temperatures to model maser emission (see Appendix A3). The agreement between the results was always better than 1 per cent of the maximum emission and usually significantly better than 0.1 per cent. Further comparison with analytical and numerical independent ad hoc codes to simple 2D and 3D scenarios gave emission differences always smaller than 0.5 per cent.

We fitted the observed redshifted, blueshifted and moment 0 maps. Several parameters were kept fixed in our calculations and their values were taken from the literature (Table 5). The envelope is divided into three Regions (I, II and III, outwards from the star) separated by two acceleration zones at 5 and $20R_\star$. The adopted expansion velocity field, v_{exp}, is a spherically symmetric step function of the radial distance to the star, taking a constant value of 5, 11 and 14.5 km s^{-1} in Regions I, II and III, respectively. The H_2 density profile was also spherically symmetric and $\propto r^{-2}v_{exp}^{-1}$. We assumed a line width due to turbulence and the gas kinetic temperature at the stellar surface of 5 km s^{-1}, decreasing down to 1 km s^{-1} at the inner acceleration zone following a power law, and remains constant outwards. The rotational temperatures of all the observed molecules were assumed to follow a power law depending on the distance to the star. They were taken from previous work and kept fixed during the fitting procedure since in most cases only one line per vibrational state are available in the observed data set. Regarding the spectroscopic data, the rest frequencies of the observed lines were taken from the CDMS Catalogue (Müller et al. 2005; http://www.astro.uni-koeln.de/cdms/catalog). We used the spectroscopic constants by Müller et al. (2007), Maki et al. (2000), Sanz, McCarthy & Thaddeus (2003), and Müller et al. (2012) and Izuha, Yamamoto & Saito (1994) for SiS, $H^{13}CN$, SiO, and SiC_2, respectively. The dust was assumed to be composed of amorphous carbon. The dust optical refractive indexes needed to calculate the dust emission at the observed frequencies ($n \simeq 2.6$ and $k \simeq 0.071$ at

Table 5. Fixed parameters used in the molecular fits.

Parameter	Value	Units	Ref.
D	123	pc	2
$\dot{M}$	2.0×10^{-5}	$M_{\odot}\,yr^{-1}$	3
$T_{\star}$	2330	K	4
$\alpha_{\star}$	0.02	arcsec	3
$R_{\star}$	3.7×10^{13}	cm	
R_{in}	5	$R_{\star}$	5
R_{out}	20	$R_{\star}$	5
v_{exp}(Region I)	5	$km\,s^{-1}$	5
v_{exp}(Region II)	11	$km\,s^{-1}$	5
v_{exp}(Region III)	14.5	$km\,s^{-1}$	5
$\Delta v(r = R_{\star})$	5	$km\,s^{-1}$	3
$\Delta v(r > R_{in})$	1	$km\,s^{-1}$	3
$T_{rot}(H^{13}CN; \text{Regions I-II})$	$T_{\star}(R_{\star}/r)^{0.58}$		5
$T_{rot}(H^{13}CN; \text{Region III})$	$T_{out}(R_{out}/r)$		5
$T_{rot}(SiO; \text{Regions I-III})$	$T_{\star}(R_{\star}/r)^{0.55}$		3
$T_{rot}(SiC_2; \text{Regions I-II})$	$T_{\star}(R_{\star}/r)^{0.81}$		6
$T_{rot}(SiC_2; \text{Region III})$	T_{out}		6
τ_{dust}(257GHz)	1.5×10^{-3}		1
$T_{dust}(r = R_{in})$	830	K	1
γ_{dust}	0.375		3

D: distance to the star; $\dot{M}$: mass-loss rate; $T_{\star}$: effective stellar temperature; $\alpha_{\star}$: angular stellar radius; $R_{\star}$: linear stellar radius; R_{in} and R_{out}: positions of the inner and outer acceleration zones; v_{exp}: expansion velocity field; Δv: line width ($\propto R_{\star}/r$); T_{rot}: rotational temperature; $T_{out} = T_{rot}(R_{out})$ for each molecule; τ_{dust}: optical depth of dust; T_{dust} and γ_{dust}: temperature of the dust grains at the inner acceleration shell and exponent of the power-law $T_{dust}(R_{in}/r)^{\gamma_{dust}}$. The temperature of the dust grains at R_{in} and the optical depth at 257 GHz have been estimated by fitting the observations carried out by *ISO*/SWS in the mid-infrared range (Cernicharo et al. 1999) keeping fixed γ_{dust}. It is assumed that there is no dust in Region I. (1) This work (2) Groenewegen et al. (2012) (3) Agúndez et al. (2012) (4) Ridgway & Keady (1988) (5) Fonfría et al. (2008) (6) Cernicharo et al. (2010).

257 GHz) were estimated by linear extrapolation from the results by Suh (2000) at wavelengths up to 1 mm.

The parameters for each molecular line varied during the fitting procedure were the abundance with respect to H_2 and the vibrational temperature at 5, 20 and $50R_{\star}$ for several axial angles. Those magnitudes in Region I were allowed to depend on the axial angles but they did not depend on the distance to the star, since the angular resolution of our observations is not high enough to resolve this region. All the parameters were adopted to be independent of the polar angle in front of and behind the star reflecting the low spectral resolution of the observations but they can be different in both hemispheres, i.e. the derived 3D abundance and vibrational temperature distributions are composed of two 2D distributions depending on the distance to the star and the axial angle. The number of axial angles used ranged from 9 to 12. The parameters were found to be statistically significant within a confidence interval of 95 per cent or larger after applying a multivariate statistical significance test, provided the axial width of a structure is larger than $35°$ in Region I and $15°$ in Region III.

The procedure followed to fit the observed maps starts with spherically symmetric abundance and temperature distributions adopted from the literature. The redshifted, blueshifted and moment 0 emissions of all the lines of a given molecule are fitted at the same time. For each line, maps in B configuration are fitted first. The derived abundance and temperature distributions are used as initial conditions to fit the maps in BC configuration.

The fits have been performed several times adopting different starting points in the space of parameters in order to look for substantially different minima of the χ^2 function. The results of this search suggest that the solutions to the fits are not degenerated. However, the space of parameters is huge and a complete exploration would require a very large computational effort. Thus, we might have overlooked other different solutions that also describe the observations.

The synthetic and observed brightness distributions usually differ in less than 1σ and always in less than 2σ, where σ is the rms noise level of the observed image. The uncertainties of the abundances and the vibrational temperatures have been estimated by varying these magnitudes until the differences between the synthetic and the observed brightness distributions change in 1σ at any position. The error of the abundance and the vibrational temperature is between 25 per cent and a factor of 2. The parameters in Region I show the largest relative errors in both magnitudes.

4.1 SiS

The fits to the observed emission of the SiS lines have been performed assuming a circularly symmetric abundance distribution equal to 5.3×10^{-6} in Region I, which decreases linearly down to 1.6×10^{-6} and 1.3×10^{-6} at the outer acceleration shell and $50R_{\star}$, respectively, remaining constant outwards (Fonfría et al., in preparation). The adopted rotational temperature for the vibrational states $v = 0$ and 1 has been $2330(R_{\star}/r)^{0.6}$ K and the vibrational temperature, $1550(R_{\star}/r)^{0.6}$ K for band $v = 1-0$ and $1300(R_{\star}/r)^{0.6}$ K for band $v = 2-1$ and those involving higher vibrational states. Under these conditions, the thermal emission accounts only for a maximum of 30 per cent of the observed flux density of line SiS($v = 0$, $J = 14-13$). More complex models such as a point-like or an arc-like maser emitting regions and a thermal emitting halo can barely reproduce the region around the peak emission of this line but fail to fit the rest of the distribution. The synthetic emission deviates from the observed in more than 3σ in a significant fraction of the mapped area. The observed emission can be properly fitted with a set of arc-like maser emitting regions composed of gas with an expansion velocity projected upon the LoS between -12 and $12\,km\,s^{-1}$ and a weak circularly symmetric thermal contribution, mostly coming from Regions I and II (Fig. 5). The radii of the arcs in the plane of the sky range from 4 to $15R_{\star}$ (i.e. an angular distance of 80–300 mas) and their fluxes decrease with the distance to the star. Most of the emission comes from the Northern hemisphere and is produced close to the inner acceleration shell. Maser emission depends largely on the size and depth of the emitting region. Nonetheless, the SiS maser emitting structure is unresolved with the present observations and the depth of the arcs cannot be reliably estimated. This prevents us from deriving the SiS density and excitation temperature in the proposed structure.

Line SiS($v = 1$, $J = 14-13$) cannot be reproduced either assuming thermal emission with the adopted abundance and temperature distributions. The synthetic emission is about 60 per cent smaller than the observed brightness distribution. No variation in the vibrational temperature significantly improves the quality of the fit. We address this issue in Section 5.2.

4.2 H^{13}CN

The H^{13}CN abundance averaged on the axial and polar angles, $\langle x \rangle_{\varphi\theta}$, decreases by a factor of 2–3 from the stellar surface to the outer
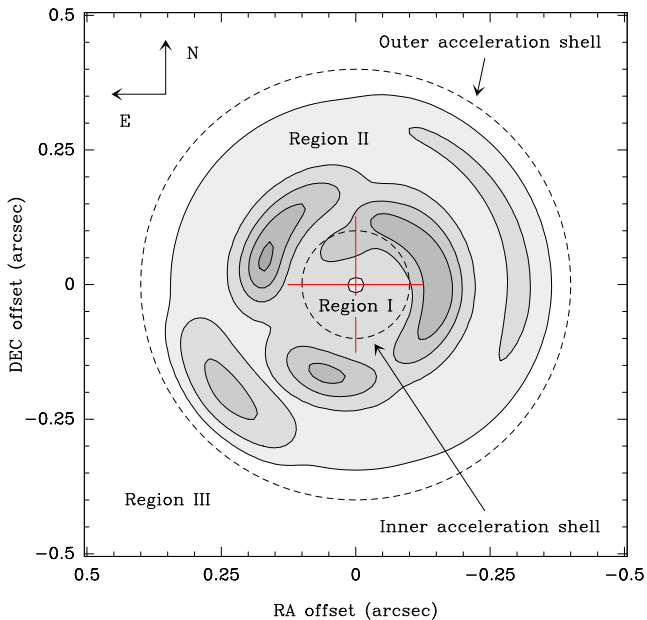
Figure 5. Moment 0 emission fitting the observed brightness distribution of line SiS($v = 0$, $J = 14–13$). The brightness distribution has been computed convolving the synthetic emission with a Gaussian beam of HPBW = 50 mas. The red cross and the dashed circles mark the positions of the central star and the acceleration zones at 5 and $20R_\star$, respectively. The plotted contours are at 3.0, 6.5, 20, 50 and 90 per cent of the peak emission ($\simeq 29.8$ Jy beam^{-1}).

Table 6. Average abundance profiles, $\langle x \rangle_{\varphi\theta}$.

Radius $(R_\star)$	$H^{13}CN$ $(\times 10^{-7})$	SiO $(\times 10^{-7})$	SiC_2 $(\times 10^{-7})$
	Moment 0 emission		
$1–5^-$	8 ± 3	$\lesssim 0.20$	8 ± 5
5^+	8 ± 3	2.4 ± 0.8	8 ± 5
20	3.3 ± 1.0	3.3 ± 1.0	0.8 ± 0.7
50	2.5 ± 0.8	1.8 ± 0.9	3.4 ± 1.7
	Redshifted emission		
$1–5^-$	9 ± 4	$\lesssim 0.25$	6 ± 4
5^+	9 ± 4	3.9 ± 1.7	6 ± 4
20	3.6 ± 1.2	4.9 ± 1.3	0.9 ± 1.1
50	3.5 ± 1.3	2.4 ± 1.7	3.8 ± 2.3
	Blueshifted emission		
$1–5^-$	5.8 ± 2.2	$\lesssim 0.30$	9 ± 6
5^+	5.8 ± 2.2	0.9 ± 0.1	9 ± 6
20	2.9 ± 0.9	1.8 ± 1.0	0.7 ± 0.5
50	1.5 ± 0.6	1.1 ± 0.6	3.0 ± 1.8

The abundances have been calculated by averaging the results of the fits on the axial and polar angles. The dispersions are the standard deviation of the data sets. The superscripts $^+$ and $^-$ indicate the approach to the inner acceleration shell from outside of Region I and from inside, respectively.

acceleration zone, remaining nearly constant outwards (Table 6). It is larger behind the star in Regions I and II.

The spatial distribution of the $H^{13}CN$ abundance (Fig. 6) reveals the presence of a bipolar structure lying along the NNE-SSW direction (PA $\simeq 15°$) that extends throughout Region I and part of Region II. The abundance in this structure due SSW is about
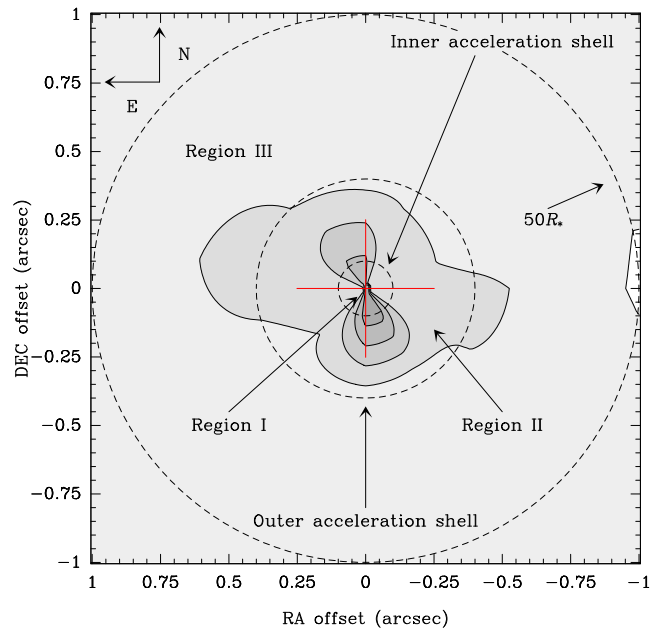

Figure 6. $H^{13}CN$ abundance with respect to H_2 averaged on the polar angle, $\langle x \rangle_\theta$. The contours are at 10, 30, 50, 70 and 90 per cent of the maximum abundance ($\simeq 1.3 \times 10^{-6}$). The red cross indicates the position of the central star. The dashed circles are at 5, 20 and $50R_\star$ from the star.

40 per cent larger than due NNE. In Region II, the $H^{13}CN$ abundance is strongly reduced by a factor of up to 6.

The $H^{13}CN$ lines in the vibrational states $v = 1$ can be fitted with a circularly symmetric vibrational temperature distribution of 2300 K in average in Region I.

4.3 SiO

The SiO average abundance $\langle x \rangle_{\varphi\theta}$ in Region I required to reproduce the emission near the star is $\lesssim 2 \times 10^{-8}$, at least one order of magnitude smaller than the abundance in Regions II and III (see Section 5.4). The maximum of the abundance profile is located at the outer acceleration zone. The fit shows that most of the SiO is located behind the star, specially in Region II (Table 6). The abundance distribution $\langle x \rangle_\theta$ shows two main SiO abundance peaks (Fig. 7). The strongest is located at the outer acceleration shell due S-SW. The other peak is found to the NE of the star at $\simeq 50R_\star$, apparently behind it.

The average vibrational temperature at the inner and outer acceleration zone is $\simeq 1750$ and 580 K, respectively. The spatial distribution of the vibrational temperature displays an elongation throughout Region III roughly due NE where it is at least a factor of 2 larger than along other directions (Fig. 8).

4.4 SiC_2

The SiC_2 average abundance $\langle x \rangle_{\varphi\theta}$ derived from our fits decreases throughout Regions I and II and increases outwards (Table 6). The abundance in front of the star is about two times larger in Region I than behind it.

The abundance distribution $\langle x \rangle_\theta$ shows a roughly semicircular structure distributed to the S of the star with a peak emission five to six times larger than due N (Fig. 9). Three increments can be noticed beyond the outer acceleration shell towards NE, SE and W
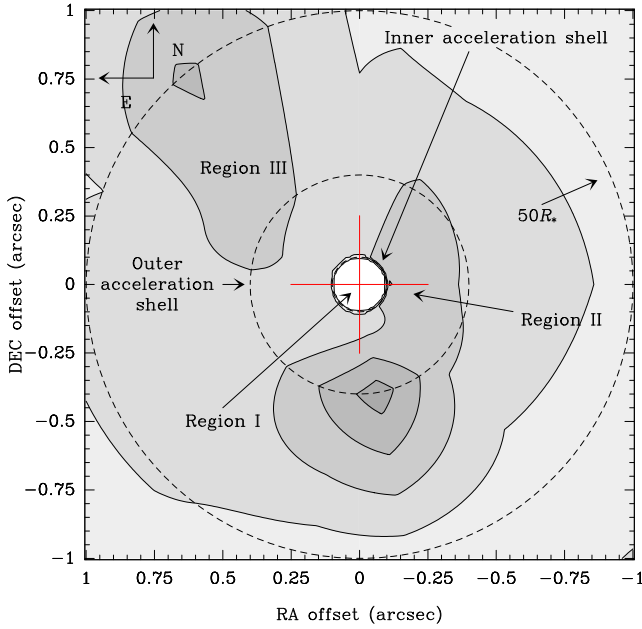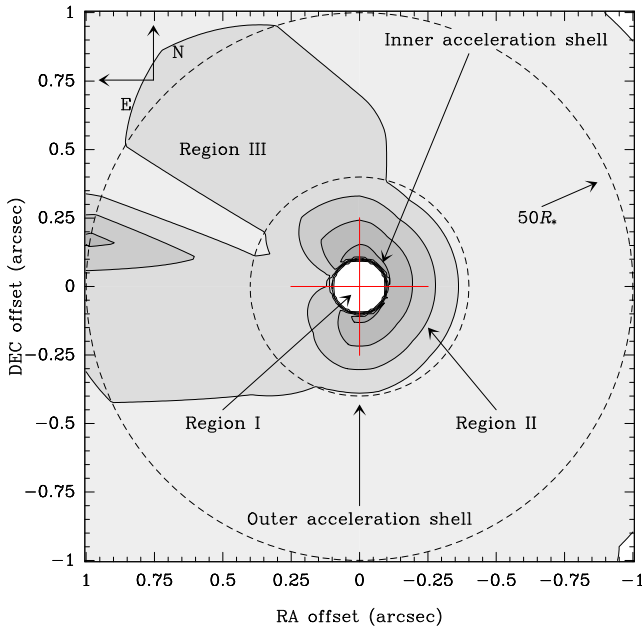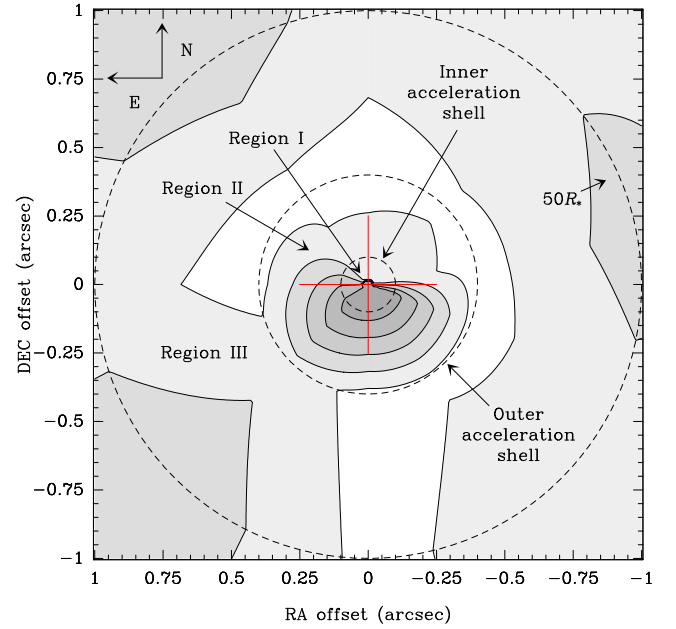
Figure 7. SiO abundance with respect to H_2 averaged on the polar angle, $\langle x \rangle_\theta$. The contours are at 10, 30, 50, 70 and 90 per cent of the maximum abundance ($\simeq 6.0 \times 10^{-7}$). The red cross indicates the position of the central star. The dashed circles are at 5, 20 and $50 R_\star$ from the star.

Figure 9. SiC_2 abundance with respect to H_2 averaged on the polar angle, $\langle x \rangle_\theta$. The contours are at 10, 30, 50, 70 and 90 per cent of the maximum abundance ($\simeq 1.4 \times 10^{-6}$). The red cross indicates the position of the central star. The dashed circles are at 5, 20 and $50 R_\star$ from the star.

5 ANALYSIS AND DISCUSSION

This work is based on interferometric observations carried out in two different CARMA configurations. Between both observations there was a period of 14 months. Following Jenness et al. (2002), the data in B and C configurations were acquired when the phase of IRC+10216 was 0.8 and 0.5, respectively. The changes in the radiation field existing in the dust formation zone during a pulsation period could largely influence the molecular excitation (e.g. Carlström et al. 1990; Monnier et al. 1998). This probably explains the differences in the continuum and most of the molecular line emission between B and C configuration observations (Table 4). However, the strong variation of the SiS emission between the two epochs seems to be related to its maser nature (see Section 5.2).

5.1 Continuum emission

In Section 3.1.2, we proposed that the continuum emission is composed of a compact source surrounded by a halo. This structure is compatible with that inferred from previous observations (Lucas 1997; Lucas & Guélin 1999; Patel et al. 2009; Shinnaga et al. 2009).

The halo is very probably produced by the dust emission coming from Region II, where most of dust is formed and its temperature is still high (e.g. Men'shchikov et al. 2001; Fonfría et al. 2008).

The compact source has a size of 50 ± 20 mas, very similar to the diameter of the star ($\simeq 30$–50 mas; Ridgway & Keady 1988; Monnier et al. 2000a; Men'shchikov et al. 2001). The flux density of the star, assumed as a blackbody with an effective temperature of 2500 K (Ridgway & Keady 1988; Ivezić & Elitzur 1996; Bergeat, Knapik & Rutily 2001; Men'shchikov et al. 2001), is $\simeq 150$ mJy at 257 GHz, i.e. a factor of $\simeq 3$ smaller than the flux density observed in B and C configurations (380 ± 60 and 530 ± 80 mJy). On the other hand, our code indicates that the dust contribution compared to the flux density of the star is negligible ($\lesssim 20$ mJy). Hence, the flux density excess may come from (i) a shell surrounding the star

Figure 8. Vibrational temperature of SiO averaged on the polar angle, $\langle T_{vib} \rangle_\theta$. The contours are at 10, 30, 50, 70 and 90 per cent of the maximum temperature ($\simeq 2000$ K). The red cross indicates the position of the central star. The dashed circles are at 5, 20 and $50 R_\star$ from the star. The temperature in Region I cannot be reliably determined from our observations.

(PA $\simeq 45°$, $135°$ and $280°$, respectively). A minimum with an abundance at least a factor of 3 smaller than for other orientations extends from the outer acceleration shell outwards due S (PA $\simeq 180°$).

The vibrational temperature can be assumed to be circularly symmetric. It is about 1700 K in Region I and is compatible with a decrease down to about 200 K at the end of Region II.

that mostly emits in the mm and probably cm wavelength ranges or (ii) from the star itself, if we assume that it does not emit as a blackbody. Both scenarios have already been invoked previously (Sahai, Claussen & Masson 1989; Menten et al. 2006, 2012).

5.2 SiS

In Section 4.1, we showed that the emission of line SiS($v = 0$, $J = 14$–13) can only be explained considering the presence of several maser emitting arcs (Fig. 5). The necessity to include maser emission in the model is directly related to the large ratio of the amplitudes in C to B configurations in the overlap range of the *uv*-plane of line SiS($v = 0$, $J = 14$–13, Table 4). It can be argued that this variation could be produced by errors in the flux calibration but, in this case, these errors would be similarly reflected in the rest of the observed lines. However, the amplitude measured for the rest of the lines in both epochs show good agreement, indicating that the SiS emission has suffered an intrinsic variation directly related to the evolution of the pumping mechanism in that period of time.

According to Fonfría Expósito et al. (2006), the most probable pumping mechanism of line SiS($v = 0$, $J = 14$–13) is produced by the overlap of certain ro-vibrational lines of SiS (that we will name excitable lines) with other of C_2H_2, HCN and their isotopologues with similar frequencies (exciting lines). The Doppler shift due to the relative motion of separate gas volumes produce a frequency shift that favours the overlap of the exciting and the excitable lines. This selective excitation mechanism could invert the population of the levels involved in a rotational transition if the intensity of the exciting radiation and the density of SiS are large enough. Thus, the maser emitting arcs derived from our fits would match up with regions where any of the following magnitudes is larger compared with their surroundings: (i) the density of SiS, (ii) the intensity of the available exciting radiation, or (iii) the overlap fraction between the exciting and the excitable lines. The last case would imply that the expansion velocity field depends on the axial angle, φ, or the turbulence velocity is larger than expected in the maser emitting regions. The strong variation in the emission found between the observations in B and C configuration is probably caused by a change in the intensity of the exciting radiation, produced by the time evolution of the excitation of C_2H_2 and HCN.

A set of maser emitting arcs is a simple structure to explain the observations, but the actual morphology is probably more complex. A continuous and inhomogeneous emitting region with a size larger than the synthesized PSF or a set of emitting clumps significantly smaller than the PSF could also produce the observed brightness distribution.

The comparison of our observation of the vibrationally excited line SiS($v = 1$, $J = 14$–13) (see Fig. 1 and Table 2) with that by Agúndez et al. (2012), acquired with the 30-m telescope, indicates that the peak flux of our observation in B configuration ($\simeq 2.25$ Jy with an HPBW $\simeq 0.25$ arcsec; Table 2) is $\simeq 20$–30 per cent larger (Agúndez et al. 2012 reported $\simeq 1.75$ Jy with an HPBW $\simeq 9.7$ arcsec). This is not possible for a steady state line and it does not happen for the rest of the lines observed in the current work, which are weaker than the single-dish observations carried out by Agúndez et al. (2012) and He et al. (2008). Thus, line SiS($v = 1$, $J = 14$–13) might change with time as other SiS lines observed towards IRC+10216 (Carlström et al. 1990). In addition, as the peak of the synthetic emission of line SiS($v = 1$, $J = 14$–13) calculated assuming thermal emission is significantly smaller than the observed ($\simeq 60$ per cent, see Section 4.1), this line could also display maser

emission, as was previously suggested by Turner et al. (1987) and He et al. (2008).

5.3 $H^{13}CN$

The abundance of $H^{13}CN$ derived from our fits agrees with the results of previous works throughout the envelope (Table 7). The difference between our abundance and that by Fonfría et al. (2008) is consequence of the lower angular resolution of their observations and the different distance to the star adopted in their model (180 pc) compared with our choice (123 pc).

In Fig. 10, we compare the density of $H^{13}CN$ derived from our fits with the results of the calculations under TE we have performed with the chemical model developed by Tejero & Cernicharo (1991). In these calculations, we have adopted the most accurate estimate of the H_2 density to date (Cernicharo et al. 2013). Both $H^{13}CN$ density profiles are compatible within our error intervals from $\simeq 3$ up to $10R_\star$, where the TE condition probably fades out. However, at the stellar surface, there is more than one order of magnitude difference between the theoretical density provided by the chemical model and the density obtained from the observations. Despite the emission
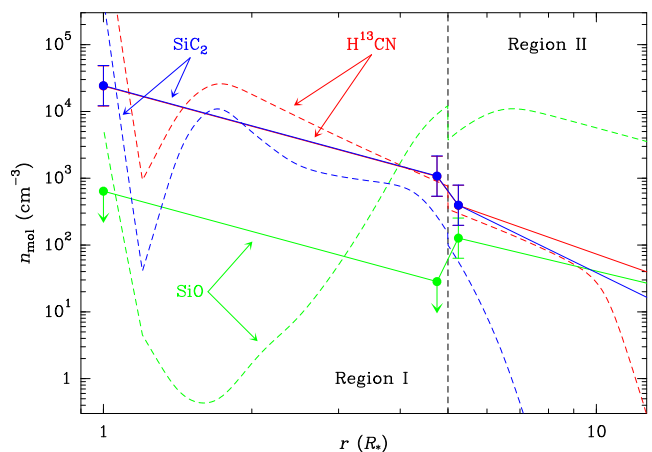
Table 7. Abundances of $H^{13}CN$.

	$r(R_\star)$			Reference
1.0–1.5	1.5–5.0	5–20	20–50	
8	8	8.0−3.3	3.3−2.5	1
13	3	1	1	2
3	3	11	5	3
4	4	4	4	4

All the abundances are multiplied by 10^{-7}. (1) This work (2) Cernicharo et al. (2011) (3) Fonfría et al. (2008) (4) Schöier et al. (2007). The data assigned to Cernicharo et al. (2011) have been calculated from their results for HCN assuming an isotopic ratio $^{12}C/^{13}C \simeq 45$ (Cernicharo et al. 2000; Kahane et al. 2000).

Figure 10. $H^{13}CN$, SiO and SiC_2 densities in Regions I and II. The results of our fits to the observed brightness distributions (Table 6) are plotted in solid lines ($H^{13}CN$ in red, SiO in green and SiC_2 in blue). The dashed curves are the results of the calculations we have performed with the chemical model developed by Tejero & Cernicharo (1991), which assumes TE and uses the most recent estimate of the H_2 density and the kinetic temperature in the dust formation zone of the envelope (Cernicharo et al. 2013). The abundances of $H^{13}CN$ and SiC_2 derived from our observations are very similar in Region I and they are superimposed.

from Region I is unresolved in our observations, a variation of an order of magnitude in the abundance at the stellar surface compared with the average value in Region I would be noticeable, as the results of our code suggest. This situation is also found for SiO and SiC$_2$, suggesting that the H$_2$ density very close to the star derived by Cernicharo et al. (2013) might be overestimated.

We derive an average vibrational temperature in Region I of 2300 K by fitting the emission of line H^{13}CN(v_2^{1e}, $J = 3-2$). This result agrees with the upper limit of the vibrational temperature $\simeq$950–2300 K, derived by Fonfría et al. (2008), and is significantly larger compared with what Cernicharo et al. (2011) suggested ($\simeq$400 K). However, these differences could be the consequence of the use of larger PSFs than ours, tracing gas mostly at the inner acceleration shell and beyond. The vibrational temperature derived in the current work would be better compared with that of the higher energy vibrational states ($\simeq$2500 K) observed by Cernicharo et al. (2011), which are very probably excited in the surroundings of the star.

The bipolar structure in Regions I and II derived from our fits reveals an overall asymmetry close to the star, where the highest abundance lays along the NNE-SSW direction with a factor of 2–3 larger than along the perpendicular direction. Hence, the formation of H^{13}CN (HCN) would be triggered by an anisotropic mechanism, probably related to the matter ejection process.

The abundance of H^{13}CN decreases monotonically from the inner to the outer acceleration shell. In Region I, significant variations in the abundance of most molecules may occur due to a variety of non-equilibrium processes (Willacy & Cherchneff 1998; Agúndez & Cernicharo 2006; Cherchneff 2006; Cernicharo et al. 2010). However, molecules such as H^{13}CN are likely chemically inactive in Region II (Cherchneff 2006) and they are not expected to play a dominant role in the process of dust formation, thus maintaining a rather constant abundance. As we have adopted in our fits, a fixed H$_2$ density profile ($\propto r^{-2}v_{exp}^{-1}$, with a constant v_{exp} out of the acceleration shells), the decrease observed in the H^{13}CN abundance with respect to H$_2$ in Region II may indicate that the actual H$_2$ density profile is steeper than what we have assumed. This could be explained if the gas expansion velocity slightly increases throughout Region II, as was previously proposed by Keady et al. (1988), Keady & Ridgway (1993) and Boyle et al. (1994).

As it was stated above, other unknown degenerate solutions to the fitting problem might reproduce the observations. The parameters are more affected by uncertainties in Region I, as long as its size is comparable to the PSF. However, these errors are not expected to severely change the overall structure of the abundance distribution in Region I. In Regions II and III, the uncertainties of the abundance are smaller and the model is more reliable. Globally, we expect a good qualitative agreement between the model and the actual abundance distribution, not only for H^{13}CN but also for SiO and SiC$_2$.

5.4 SiO

The abundances derived from our fits agree with most of the results available in the literature (Table 8). However, the abundance proposed by Keady & Ridgway (1993) from mid-IR observations is a factor of $\gtrsim$3 larger than ours throughout the envelope. These observations were also analysed by Schöier et al. (2006b) finding an abundance up to 7–8 times larger than ours in Region II. These significant disagreements could be the consequence of instrumental issues that affected these observations (Keady & Ridgway 1993).

Table 8. Abundances of SiO.

1.0–5.0	$r(R_\star)$ 5–20	20–50	Reference
$\lesssim$ 0.2	2.4$-$3.3	3.3$-$1.8	1
1.8	1.8	1.8	2
0.2–3.0	0.2–3.0	1.0	3
2.8	2.8	2.8	4
0.3–15	15–1.7	1.7	5
8.0	8.0	8.0	6

All the abundances are multiplied by 10^{-7}. (1) This work (2) Agúndez et al. (2012) (3) Decin et al. (2010b) (4) Schöier et al. (2006a) (5) Schöier et al. (2006b) (6) Keady & Ridgway (1993). Schöier et al. (2006b) also divided the envelope in three regions with different extent to ours and constant abundances. This fact accounts for the larger variations in the abundance encountered in this Table in Regions I and II. Similarly, Decin et al. (2010b) gave the abundances between the stellar surface and the shell at 8$R_\star$ and beyond.

The comparison between our estimate of the SiO density and the calculated under TE suggests that this condition only stands between the surface of the star and $\simeq$3$R_\star$ (Fig. 10). At larger distances from the star, the SiO density under TE is up to two orders of magnitude larger than that derived from our observations suggesting the evolution of the SiO abundance is controlled by chemical kinetics, as was already proposed by Agúndez & Cernicharo (2006).

The deficit of SiO emission in front of the star noticed in the moment 0 and the blueshifted emission maps (about 20 per cent of the expected emission; Figs 3 and 4) and directly related to a significant decrease in the SiO abundance in Region I in our fit (Section 4.3) could be argued to be also the effect of (i) self-absorption or (ii) absorption of the continuum emission coming from the star by SiO. Self-absorption is produced mostly along the LoS due to absorption of the radiation emitted by the warm gas in Region I by the colder gas in Regions II and III. The different expansion velocity of the gas in Region I and Regions II and III (5 km s^{-1} against 11 and 14.5 km s^{-1}, respectively, Section 1.1), allow the gas in Regions II and III to absorb less than 5 per cent of the emission coming from Region I (adopting the abundance in Regions II and III from Table 8 and an abundance for Region I equal to that for Region II). Since the HPBW of the PSF of our observations in B configuration ($\simeq$0.25 arcsec) is more than six times larger than the size of the central star of IRC+10216 ($\simeq$0.04 arcsec), this process cannot be the responsible of the evident emission deficit in our observation. Regarding the second case, the stellar emission, which accounts for the bulk of the continuum (Section 5.1), is absorbed by the SiO in front of the star. This absorption is not removed from the molecular observations with the continuum and could substantially modify the SiO emission in the moment 0 and blueshifted maps. Our code indicates that any modification in the SiO abundance in Regions II and III produces a negligible emission deficit in these maps. However, significant absorptions could arise from, e.g. dense cold clumps in front of the star located in Region I.

The strong increase of one order of magnitude observed in the abundance between Regions I and II occurs around the inner acceleration zone, where dust grains are formed and grow. The chemical reaction usually invoked to explain the formation of SiO in gas-phase in the innermost envelope of C-rich AGB stars is Si+CO→SiO+C,

efficient at high kinetic temperatures and high density (Willacy & Cherchneff 1998; Agúndez & Cernicharo 2006; Cherchneff 2006; Agúndez et al. 2012). Under these conditions, the chemical models predict an increase of 1–2 orders of magnitude in the SiO abundance from the stellar photosphere up to roughly the inner acceleration shell, in very good agreement with our results.

The possible acceleration undergone throughout Region II by the gas inferred from the analysis of the $H^{13}CN$ abundance would also affect the abundance distribution derived from the SiO emission. The small difference between the abundance at the inner and outer acceleration shells resulting from our fits (Table 8), performed assuming a constant gas expansion velocity in Region II, could be an effect of the uncertainties of the fitting procedure. However, the existence of a gas acceleration in Region II would enhance this abundance difference suggesting that SiO may be formed also throughout this Region but at a lower rate than in the inner acceleration zone.

The SiO vibrational temperature averaged on the polar angle derived from our fits (1750 and 580 K in the inner and outer acceleration shells) is larger than the kinetic temperature ($\simeq 950$ and 450 K; Agúndez et al. 2012). Thus, SiO is vibrationally out of LTE throughout the dust formation zone, mostly around the inner acceleration shell, where the bulk of SiO is formed. The increment in the vibrational temperature found roughly along NE suggests the existence of an excitation mechanism which is not working in the rest of the envelope. This mechanism may involve (i) a selective excitation of the observed SiO line, or (ii) shocks or a strong IR or UV radiation field, which would affect the rest of the molecules as well. New observations of the $H^{13}CN$, SiS and SiC_2 vibrationally excited lines at $\simeq 0.7$ arcsec resolution may help to solve this dichotomy.

5.5 SiC_2

The SiC_2 abundance averaged on the axial and polar angles, $\langle x \rangle_{\varphi\theta}$, decreases by an order of magnitude from the inner to the outer acceleration zone, and then increases by a factor of 4 throughout Region III (Table 6). The decrease we observe across Region II is probably produced by depletion of SiC_2 on to dust grains due to the refractory character of this Si-bearing molecule. This depletion and the subsequent growth of the dust grains could enlarge their cross-section enough to significantly increase the force produced by the stellar radiation pressure on them, accelerating the dust grains. The dust grains, dynamically coupled to the gas in Region II due to its still high density, would also accelerate the gas, as we have suggested from the analysis of the abundance profile of $H^{13}CN$ (Section 5.3).

Our estimate of the average SiC_2 abundance in Region I agrees with most of the results derived from previous observations (Table 9), with the abundance estimated with chemical models under TE ($3–5 \times 10^{-7}$; Willacy & Cherchneff 1998; Cernicharo et al. 2010), and with that calculated by us also under TE between $\simeq 1.5$ and $4R_\star$ (Fig. 10). Our fits suggest that the SiC_2 abundance in Region I and II is larger due S than due N by a factor of 5–6. The SiC_2 peak abundance is located to the S of the star, as in the case of $H^{13}CN$. This fact support the idea of an anisotropic mechanism driving the chemistry close to the star.

The increase experienced by the SiC_2 abundance in Region III might be explained by (i) the activation of a gas-phase chemical reaction or (ii) evaporation of SiC_2 molecules adsorbed to the dust grains across Regions I and II due to desorption processes such as grain–grain or molecule–grain collisions, or photodesorption triggered by the action of Galactic UV radiation penetrating across a clumpy envelope (Agúndez et al. 2010; Decin et al. 2010a). More-

Table 9. Abundances of SiC_2.

	$r(R_\star)$		Reference
1.0–5.0	5–20	20–50	
8	8.0−0.8	0.8−3.4	1
−	−	2.0−2.9	2
5	5	5	3
$\lesssim 0.5$	$\lesssim 0.5$	$\lesssim 0.5$	4

All the abundances are multiplied by 10^{-7}. (1) This work (2) Cernicharo et al. (2010) (3) Lucas et al. (1995) (4) Gensheimer et al. (1995). Cernicharo et al. (2010) derived the abundance of SiC_2 only at distances from the star larger than 0.5 arcsec, i.e. $25R_\star$ for us.

over, the SiC_2 depletion process on to the dust grains suggested to be working throughout Region II would become less efficient at larger distances to the star as the gas density decreases and the expansion velocity of the dust grains grows compared to that of the gas. Since the gas depletion is a dynamical process, inefficient desorption mechanisms in Regions I and II could play a major role in Region III.

5.6 Remarkable directions in the envelope

Fig. 11 shows the relative abundance distribution of $H^{13}CN$, SiO and SiC_2. These maps have been obtained by dividing the abundance distributions by the abundance averaged on the axial and polar angles. The relative abundance distributions of all the molecules show strong features along directions NE and S-SW. The $H^{13}CN$ and SiO relative abundances display an excess towards these two directions, while the SiC_2 one shows a deficit.

The NE and S-SW directions are compatible with the NE–SW direction of the axis found in the dusty component of the envelope (Dyck et al. 1987; Ridgway & Keady 1988; Kastner & Weintraub 1994; Sloan & Egan 1995; Skinner, Meixner & Bobrowsky 1998; Haniff & Buscher 1998; Weigelt et al. 1998, 2002; Osterbart et al. 2000; Tuthill et al. 2000; Tuthill, Monnier & Danchi 2005; Leão et al. 2006). From observations covering the dust formation zone, Men'shchikov et al. (2001, 2002) derived the existence of two cavities along this axis with an overall size $\simeq 0.5$ arcsec. The opening angle and inclination of the cavities are $\simeq 40°$ and $\simeq 30°–40°$, respectively, suggesting that the cavity to the SW is in front of the star and that to the NE is behind the star. The axial size of all the strong features present in our relative abundance maps of $H^{13}CN$, SiO and SiC_2 is $\gtrsim 30°–40°$, comparable or larger than the opening angle of the cavities in the dusty component of the CSE. Most of the molecular features exist in front of and behind the star at the same time with the exception of the feature of SiO at $50R_\star$ due NE, which is located only behind the star. These facts suggest that the structures associated to the molecular features may be wrapping the cavities in the dusty component of the envelope.

Another remarkable direction in the envelope is SE, defined by a strong feature in the SiC_2 abundance distribution. However, this direction seems to be unimportant for $H^{13}CN$ and SiO. It has been associated to the region throughout the CSE with the largest density of dust grains (e.g. Dyck et al. 1987; Ridgway & Keady 1988; Men'shchikov et al. 2001; Shinnaga et al. 2009). This fact joined to the agreement between the location of the cavities in the dusty component of the envelope along the NE–SW direction and the deficit in the SiC_2 abundance might indicate that there exists a correlation between the density of dust grains and the SiC_2 abundance.
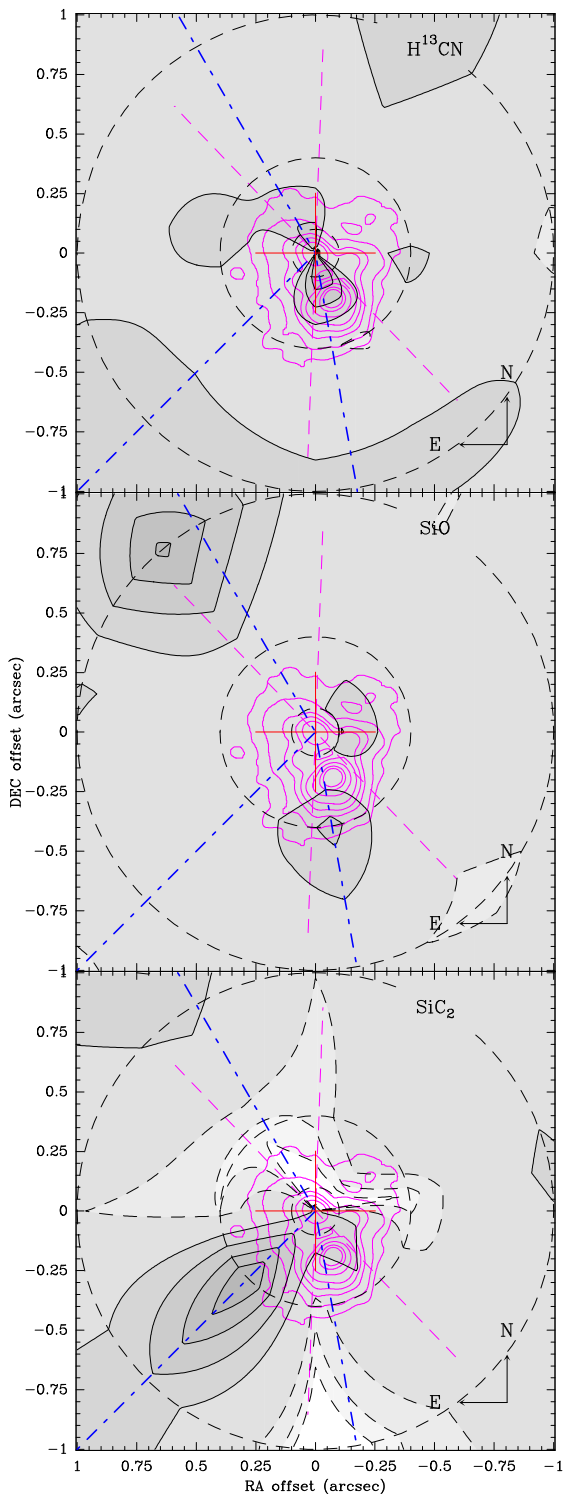
Figure 11. Ratios of the abundance distributions to those averaged on the axial and polar angles for H^{13}CN, SiO and SiC$_2$ (grey-scale and black contours). The dash–dotted straight lines (blue) represent remarkable directions (NE, S-SW and SE). The average distributions have been calculated after excluding the abundances along these directions. The dashed circles are at 5, 20 and 50$R_\star$. The solid contours are at levels 1.5, 2.0, 2.5 and 3.0. Dashed contours are at levels 0.4, 0.5 and 0.7. The contours plotted in magenta represent the continuum emission at 2.17 μm acquired with speckle-masking interferometry by Weigelt et al. (1998, Fig. 1 a in this reference). The magenta dashed lines define the cavities in the dusty component derived by Men'shchikov et al. (2001, 2002).

6 CONCLUSIONS

IRC+10216 has been observed at 1.2 mm with the CARMA interferometer in B and C configurations. The angular resolution is one of the largest ever achieved regarding molecular observations towards this source (HPBW $\gtrsim$ 0.25 arcsec). The available band width allowed us to observe the continuum emission and several lines of SiS, H^{13}CN, SiO and SiC$_2$ with enough SNR to perform a reliable analysis. The main conclusions of this work are as follows.

(i) The brightness distribution of line SiS($v = 0, J = 14$–13) was reproduced assuming that most of the emission comes from several maser emitting arcs. The SiS flux measured from our two separated observations changed dramatically, supporting the idea of a maser origin for the SiS emission.

(ii) The abundance of H^{13}CN with respect to H$_2$ shows a bipolar structure along the NNE-SSW direction in Regions I and II. In average, it undergoes a significant decrease between the inner and outer acceleration shells. The vibrational temperature close to the star is about 700 K in average larger than was previously suggested.

(iii) The SiO appears mostly in the inner acceleration shell. Inwards, its abundance is at least one order of magnitude smaller than for the rest of the envelope. Most of the SiO is located behind the star. The vibrational temperature indicates that SiO is vibrationally out of LTE between the inner and outer acceleration shells. A substantial increment of this magnitude has been found around the NE compared to other directions.

(iv) The abundance of SiC$_2$ shows a significant minimum located at the outer acceleration zone, probably produced by depletion on to dust grains. A further increase in the abundance has been detected beyond the outer acceleration shell. Most of the SiC$_2$ is located towards the S of the star in Regions I and II.

(v) The abundance distributions of H^{13}CN, SiO and SiC$_2$ are irregular and show remarkable directions along which the abundances are significantly different from the rest of the envelope. These directions are NE, S-SW and SE. The directions NE and S-SW match up with the axis of the dusty component of the envelope (NE–SW), previously inferred from continuum observations. The direction SE coincides with that associated to the region of the envelope with the largest amount of dust. The abundance of SiC$_2$ seems to be correlated with the density of dust grains.

REFERENCES

Agúndez M., Cernicharo J., 2006, ApJ, 650, 374
Agúndez M., Cernicharo J., Guélin M., 2010, ApJ, 724, L133
Agúndez M., Fonfría J. P., Cernicharo J., Kahane C., Daniel F., Guélin M., 2012, A&A, 543, 48

Becklin E. E., Frogel J. A., Hyland A. R., Kristian J., Neugebauer G., 1969, ApJ, 158, 133

Bergeat J., Knapik A., Rutily B., 2001, A&A, 369, 178

Bieging J. H., Nguyen-Quang-Rieu, 1989, ApJ, 343, L25

Bieging J. H., Tafalla M., 1993, AJ, 105, 576

Boyle R. J., Keady J. J., Jennings D. E., Hirsch K. L., Wiedemann G. R., 1994, ApJ, 420, 863

Briggs D. S., 1995, PhD thesis, The New Mexico Institute of Mining and Technology

Briggs D. S., Schwab F. R., Sramek R. A., 1999, in Taylor G. B., Carilli C. L., Perley R. A., eds, ASP Conf. Ser.Vol. 180, Synthesis Imaging in Radio Astronomy II. Astron. Soc. Pac., San Francisco, p. 127

Carlström U., Olofsson H., Johansson L. E. B., Nguyen-Q-Rieu Sahai R., 1990, in Mennessier M. O., Omont A., eds., From Miras to Planetary Nebulae. Editions Frontieres, Gif sur Yvette, p. 170

Cernicharo J., Yamamura I., González-Alfonso E., de Jong T., Heras A., Escribano R., Ortigoso J., 1999, ApJ, 526, L41

Cernicharo J., Guélin M., Kahane C., 2000, A&AS, 142, 181

Cernicharo J. et al., 2010, A&A, 521, L8

Cernicharo J., Agúndez M., Kahane C., Guélin M., Goicoechea J. R., Marcelino N., De Beck E., Decin L., 2011, A&A, 529, L3

Cernicharo J., Daniel F., Castro-Carrizo A., Agúndez M., Marcelino N., Joblin C., Goicoechea J. R., Guélin M., 2013, ApJ, 778, 25

Cherchneff I., 2006, A&A, 456, 1001

Daniel F., Cernicharo J., 2008, A&A, 488, 1237

Decin L. et al., 2010a, Nature, 467, 64

Decin L. et al., 2010b, A&A, 518, L143

Downes D. et al., 1999, A&A, 347, 809

Drake S. A., Linsky J. L., Judge P. G., Elitzur M., 1991, ApJ, 483, 913

Dullemond C. P., Turolla R., 2000, A&A, 360, 1187

Dyck H. M., Zuckerman B., Howel R. R., Beckwith S., 1987, PASP, 99, 99

Dyck H. M., Benson J. A., Howell R. R., Joyce R. R., Leinert Ch., 1991, AJ, 102, 200

Fonfría Expósito J. P., Agúndez M., Tercero B., Pardo J. R., Cernicharo J., 2006, ApJ, 646, L127

Fonfría J. P., Cernicharo J., Richter M. J., Lacy J. H., 2008, ApJ, 673, 445

Fonfría J. P., Cernicharo J., Richter M. J., Lacy J. H., 2011, ApJ, 728, 43

Gensheimer P. D., Likkel L., Snyder L. E., 1995, ApJ, 439, 445

González-Alfonso E., Cernicharo J., 1993, A&A, 279, 506

Groenewegen M. A. T. et al., 2012, A&A, 543, L8

Guélin M., Lucas R., Cernicharo J., 1993, A&A, 280, L19

Haniff C. A., Buscher D. F., 1998, A&A, 334, L5

He J. H., Dinh-V-Trung, Kwok S., Müller H. S. P., Zhang Y., Hasegawa T., Peng T. C., Huang Y. C., 2008, ApJS, 177, 275

Henkel C., Matthews H. E., Morris M., 1983, ApJ, 267, 184

Ivezić Ž., Elitzur M., 1996, MNRAS, 279, 1019

Izuha M., Yamamoto S., Saito S., 1994, Spectrochim. Acta, 50A, 1371

Jenness T., Stevens J. A., Archibald E. N., Economou F., Jessop N. E., Robson E. I., 2002, MNRAS, 336, 14

Jones T. J., Bryja C. O., Gehrz R. D., Harrison T. E., Johnson J. J., Klebe D. I., Lawrence G. F., 1990, ApJS, 74, 785

Kahane C., Dufour E., Busso M., Gallino R., Lugaro M., Forestini M., Straniero O., 2000, A&A, 357, 669

Kastner J. H., Weintraub D. A., 1994, ApJ, 434, 719

Kawaguchi K., Kasai Y., Ishikawa S.-I., Kaifu N., 1995, PASJ, 47, 853

Keady J. J., Ridgway S. T., 1993, ApJ, 406, 199

Keady J. J., Hall D. N. B., Ridgway S. T., 1988, ApJ, 326, 832

Le Bertre T., 1992, A&AS, 94, 377

Leão I. C., de Laverny P., Mékarnia D., De Medeiros J. R., Vandame B., 2006, A&A, 455, 187

Loup C., Forveille T., Omont A., Paul J. F., 1993, A&AS, 99, 291

Lucas R., 1997, Ap&SS, 251, 247

Lucas R., Guélin M., 1999, in Bertre T. Le, Lebre A., Waelkens C., eds, IAU Symp. 191, Asymptotic Giant Branch Stars. Univ. Chicago Press, Chicago, IL, p. 305

Lucas R., Guélin M., Kahane C., Audinos P., Cernicharo J., 1995, Ap&SS, 224, 293

Maki A. G., Mellau G. Ch., Klee S., Winnewisser M., Quapp W., 2000, J. Mol. Spectrosc., 202, 67

Males J. R., Close L. M., Skemer A. J., Hinz P. M., Hoffmann W. F., Marengo M., 2012, ApJ, 744, 133

Maness H. L., Fitzgerald M. P., Paladini R., Kalas P., Duchene G., Graham J. R., 2008, ApJ, 686, L25

Melnick G. J., Neufeld D. A., Saavik Ford K. E., Hollenbach D. J., Ashby M. L. N., 2001, Nature, 412, 160

Men'shchikov A. B., Balega Y., Blöcker T., Osterbart R., Weigelt G., 2001, A&A, 368, 497

Men'shchikov A. B., Hofmann K.-H., Weigelt G., 2002, A&A, 392, 921

Menten K. M., Reid M. J., Krügel E., Claussen M. J., Sahai R., 2006, A&A, 453, 301

Menten K. M., Reid M. J., Kamiński T., Claussen M. J., 2012, A&A, 543, 73

Menut J.-L. et al., 2007, MNRAS, 376, L6

Monnier J. D., Geballe T. R., Danchi W. C., 1998, ApJ, 502, 833

Monnier J. D., Danchi W. C., Hale D. S., Lipman E. A., Tuthill P. G., Townes C. H., 2000a, ApJ, 543, 861

Monnier J. D., Danchi W. C., Hale D. S., Tuthill P. G., Townes C. H., 2000b, ApJ, 543, 868

Müller H. S. P., Schlöder F., Stutzki J., Winnewisser G., 2005, J. Mol. Struct., 742, 215

Müller H. S. P. et al., 2007, Phys. Chem. Chem. Phys., 9, 1579

Müller H. S. P., Cernicharo J., Agúndez M., Decin L., Encrenaz P., Pearson J. C., Teyssier D., Waters L. B. F. M., 2012, J. Mol. Spectrosc., 271, 50

Neufeld D. A. et al., 2011, ApJ, 727, L28

Osterbart R., Balega Y., Blöcker T., Men'shchikov A., Weigelt G., 2000, A&A, 357, 169

Patel N. A. et al., 2009, ApJ, 692, 1205

Richichi A., Chandrasekar T., Leinert Ch., 2003, New Astron., 8, 507

Ridgway S. T., Keady J. J., 1988, ApJ, 326, 843

Sahai R., Claussen M. J., Masson C. R., 1989, A&A, 220, 92

Sanz M. E., McCarthy M. C., Thaddeus P., 2003, J. Chem. Phys., 119, 11715

Schöier F. L., Olofsson H., Lundgren A. A., 2006a, A&A, 454, 247

Schöier F. L., Fong D., Olofsson H., Zhang Q., Patel N., 2006b, ApJ, 649, 965

Schöier F. L., Fong D., Bieging J. H., Wilner D. J., Young K., Hunter T. R., 2007, ApJ, 670, 766

Shinnaga H. et al., 2009, ApJ, 698, 1924

Skinner C. J., Meixner M., Bobrowsky M., 1998, MNRAS, 300, L29

Sloan G. C., Egan M. P., 1995, ApJ, 444, 452

Suh K.-W., 2000, MNRAS, 315, 740

Takano S., Shaito S., Shuji T., 1992, PASJ, 44, 469

Tejero J., Cernicharo J., 1991, Modelos de equilibrio termodinámico aplicados a envolturas circunestelares de estrellas evolucionadas. IGN, Madrid

Turner B. E., 1987, A&A, 183, L23

Tuthill P. G., Monnier J. D., Danchi W. C., López B., 2000, ApJ, 543, 284

Tuthill P. G., Monnier J. D., Danchi W. C., 2005, ApJ, 624, 352

van der Tak F. F. S., Black J. H., Schöier F. L., Jansen D. J., van Dishoeck E. F., 2007, A&A, 468, 627

van Zadelhoff G.-J. et al., 2002, A&A, 395, 373

Weigelt G., Balega Y., Blöcker T., Fleischer A. J., Osterbart R., Winters J. M., 1998, A&A, 333, L51

Weigelt G., Balega Y. Y., Blöcker T., Hofmann K.-H., Men'shchikov A. B., Winters J. M., 2002, A&A, 392, 131

Willacy K., Cherchneff I., 1998, A&A, 330, 676

Witteborn F. C., Strecker D. W., Erickson E. F., Smith S. M., Goebel J. H., Taylor B. J., 1980, ApJ, 238, 577

Young K. H. et al., 2004, ApJ, 616, L51

APPENDIX A: DETAILS OF THE NUMERICAL CODE

The code used in the current work is an improved 3D version of the 1D code developed by Fonfría et al. (2008) capable of reproducing

the molecular and continuum emissions that come from symmetric or asymmetric circumstellar envelopes composed of expanding gas and dust. Our code solves the radiation transfer equation along the LoS for a number of positions in the plane of the sky and produces synthetic line emission data cubes adopting a given physical and chemical model for the envelope, i.e. the H_2 density, molecular abundance, gas expansion velocity, line width, and rotational and vibrational temperature spatial distributions. The procedure followed to perform the calculations *does not* rely on the large velocity gradient approximation and the code is well adapted to model the emission of the inner layers of the envelope, where the gas density and the temperatures are high, and the expansion velocity gradient is supposed to be small. In this Section, we benchmark this new version of the code.

A1 Gridding and sampling of the physical and chemical magnitudes

The system composed of the central star and the circumstellar envelope is described by spherical coordinates. The envelope is divided into concentric shells centred on the star in order to sample the magnitudes describing the physical and chemical conditions. To solve the radiation transfer equation, the envelope is discretized into a set of right cylinders with their axes matching up with the LoS passing through the central star. The combination of both structures gives rise to a set of annular regions parallel to the plane of the sky. A number of *principal* axial or position angles, φ, are selected to define the same number of sets of sections of the annular regions or *cells*. In each of these sets of cells, any physical or chemical magnitude is sampled depending on the distance to the star, r, and the polar angle, θ. The length of each cell along the LoS is controlled by the number of shells. The radiation transfer equation is solved along the LoS for every principal axial angle and impact parameter. The emission for any other axial angle is calculated by linear interpolation. The number of shells and principal axial angles are chosen to produce maps independent on the sampling within an error of 10 per cent of the observational uncertainty. About 100 shells and 9–12 principal axial angles have been required to reproduce the observations presented in the current paper.

A2 A brief description of the program

Contrarily to many other codes developed to reproduce the emission of circumstellar envelopes or molecular clouds (e.g. González-Alfonso & Cernicharo 1993; Dullemond & Turolla 2000; van Zadelhoff et al. 2002; van der Tak et al. 2007; Daniel & Cernicharo 2008), our code does not solve the SE. The number of levels involved in the calculations regarding the warmest regions of the envelopes of AGB stars ($T_k \simeq 1000$–3000 K) ranges between several hundred for the lightest molecules (e.g. CO, SiS, SiO, CS) to several thousand for more complex species (e.g. H_2O, HCN, C_2H_2, C_2H_4). Resolving the SE for such an environment is a very challenging task due to the lack of collisional coefficients and the huge computing effort demanded. Hence, we compute the populations of the molecular levels assuming a Boltzmann distribution with rotational and vibrational temperatures depending on the ro-vibrational quantum numbers. The partition function, necessary to calculate the opacity of the lines to be modelled, is computed by direct summation over all the considered levels. Its accuracy depends on the molecule and the uncertainty is usually 1–5 per cent for diatomic, linear and symmetric molecules, and up to 10–15 per cent for asymmetric molecules as a

consequence of the complexity of the calculations and the lack of spectroscopic constants in the literature.

Once the populations of all the required levels are calculated throughout the whole envelope, the radiation transfer equation is solved along the LoS assuming that the physical and chemical magnitudes in each cell of the grid are constant. Hence, the intensity emerging from a given point in the plane of the sky is

$$I_\nu = B_\nu(T_{CMB})e^{-\sum_{j=1}^{n}\tau_{\nu,j}} + \sum_{i=1}^{n} S_{\nu,i}\left(1 - e^{-\tau_{\nu,i}}\right)e^{-\sum_{j=1}^{i-1}\tau_{\nu,j}},$$
(A1)

where we have considered the cosmic microwave background (CMB) continuum and n is the number of cells along the LoS at that point in the plane of the sky. The source function, S_ν, and the optical depth, τ_ν, are evaluated in every cell, where the first and nth cells are the closest and farthest cells to Earth, respectively. The optical depth and the source function are defined as

$$\tau_\nu = \sum_{i=1}^{m} \tau_{\nu,i}$$
(A2)

and

$$S_\nu = \sum_{i=1}^{m} \frac{k_{\nu,i}}{\sum_{j=1}^{m} k_{\nu,j}} B_{\nu,i},$$
(A3)

where m is the number of lines of a single molecule to be reproduced and k_ν is the line opacity. All the magnitudes in these equations depend on the rotational and vibrational temperatures, and on the gas expansion velocity. The addition of more molecules or dust is straightforward. This approach allows for a correct modelling of blended lines regardless of any velocity gradient or the effect of dust on the molecular emission, important in the mid-infrared range. Moreover, our code is able to compute thermal or maser emission from any point of the envelope just by choosing the correct rotational temperatures, that can be negative.

A3 Benchmarking

The performance of our code has been analysed assuming different symmetries (1D, 2D and 3D) by comparing the results with those of ad hoc codes for simple scenarios or with those obtained from a non-local, non-LTE code (Daniel & Cernicharo 2008). The uncertainties for the 1D and 2D problems are defined for all the comparisons below as $(F_{ours} - F_{control})/\max(F_{control})$, where F_X is the emitted flux, X is the code (ours or the control codes ad hoc or DC, i.e. Daniel & Cernicharo 2008), and $\max(F_{control})$ is the maximum value of the flux calculated with the control code.

A3.1 1D problem

The abundance and temperatures are allowed to vary with the distance to the star, r. Three scenarios involving thermal and maser emission have been used to compare the results of our code with partially analytical solutions to simple problems (Scenario 1 for thermal emission and Scenario 2 for maser emission) and with totally numerical results of the non-local non-LTE code developed by Daniel & Cernicharo (2008, Scenario 3, thermal emission).

Scenario 1: we have calculated the emission of a test line ($A_{ul} = 10^{-8}$ s^{-1}, $B = 3$ cm^{-1}, $J = 1$–0) from an isothermal spherically symmetric envelope assuming LTE, $T_k = 100$ K, an H_2 density profile following the power law $r^{-\alpha}$, where $\alpha = 0, \ldots, 4$, and thermal
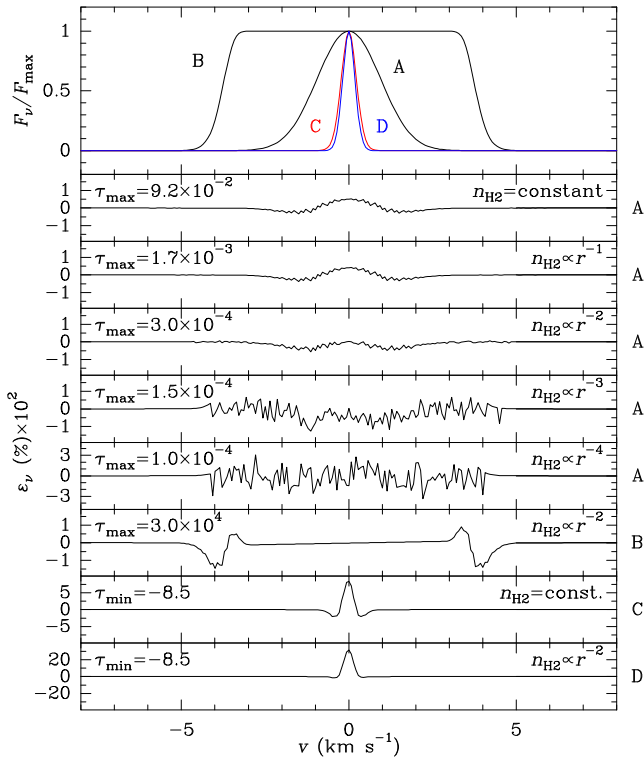
Figure A1. Test line normalized emission from a static isothermal spherically symmetric cloud depending of the H₂ density profile. The upper insert contains the emission for the optically thin (A) and optically thick (B) thermal emission and for the maser emission (C, in red, and D, in blue). The line profile in the thermal optically thin case is independent of the H₂ density. The maximum flux for the thermal lines ranges between 3×10^{-6} and 2.5 Jy, and between 5×10^{7} and 10^{8} Jy for the maser lines. All the spectra have been calculated with an ad hoc code developed for this purpose. The optical depth for every impact parameter has been analytically calculated. The continuum due to the CMB has been removed. The residuals, ε_ν, are defined as $(F_{ours} - F_{ad\text{-}hoc})/\max(F_{ad\text{-}hoc})$, where $F_{ad\text{-}hoc}$ and F_{ours} are the synthetic fluxes calculated with the ad hoc code and ours, respectively.

line width ($\simeq 2.14$ km s^{-1}; Fig. A1, lines A and B). The maximum optical depth ranged from 10^{-4} to 0.1. An extremely optically thick case ($\tau_{max} \simeq 3 \times 10^{4}$) has been also considered with a H₂ density profile $\propto r^{-2}$. The optical depth for every impact parameter has been analytically calculated. The convolution of the emission with an HPBW =1 arcsec has been performed numerically with the trapezoidal rule. The code accurately computes the emission from clouds with significantly different H₂ density profiles independently of the optical depth, even in the extremely optically thick regime. The results of our code deviate from the control solutions in less than 0.01 per cent.

Scenario 2: we have calculated the emission of the test line from the same cloud than in Scenario 1 but assuming an excitation temperature of −100 K for the modelled line throughout the whole cloud (Fig. A1, lines C and D). The minimum optical depth was −8.5. The optical depth has been computed analytically. In spite of the large emission of the line, with a maximum ranging between 5×10^{7} and 10^{8} Jy, the relative error is smaller than 0.4 per cent.

Scenario 3: we have calculated the emission of the hyperfine structure of lines H¹³CN($v = 0$, $J = 1$–0) and H¹³CN($v = 0$, $J = 2$–1) coming from an isothermal spherically symmetric envelope with
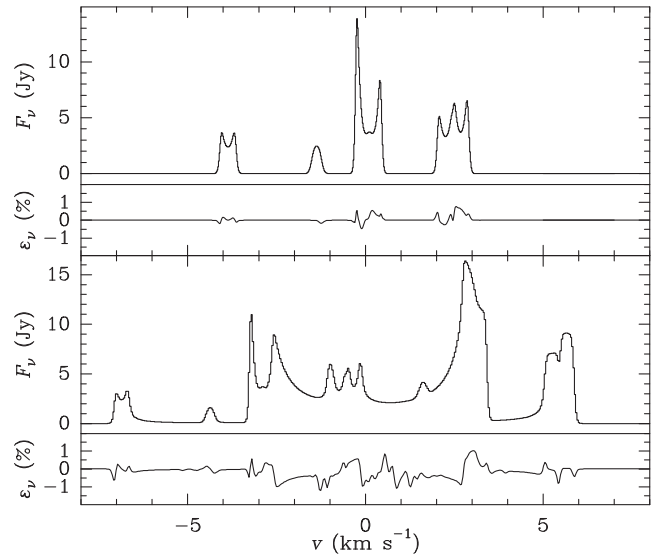

Figure A2. Hyperfine structure of line H¹³CN($v = 0$, $J = 2$–1) towards a spherically symmetric cloud expanding at 0 and 3 km s^{-1} (upper and lower inserts, respectively). See the text for a description of the physical and chemical properties of the cloud. The plotted spectra have been calculated with the non-local, non-LTE code developed by Daniel & Cernicharo (2008). The continuum due to the CMB has been removed. The residuals, ε_ν, are defined as $(F_{ours} - F_{DC})/\max(F_{DC})$, where F_{DC} and F_{ours} are the synthetic fluxes calculated with the code by Daniel & Cernicharo (2008) and ours, respectively.

$T_k = 10$ K and a constant H₂ density (Fig. A2). H¹³CN is out of LTE throughout the whole envelope, mostly in the outer shells. A turbulence velocity of 0.1 km s^{-1} and the thermal linewidth have been considered resulting in a total line width of $\simeq 0.2$ km s^{-1}. The expansion velocity has been assumed to be 0, 3 and 10 km s^{-1}. The maximum optical depth of the components of the hyperfine structure ranges between $\simeq 1$ and 60. Our code is capable of dealing at the same time with blended lines with quite different optical depths and properly modelling self-absorption. The results of our code differs from those of the control code in less than 1 per cent for all the components of the hyperfine structure of the modelled lines, regardless of the gas expansion velocity.

The good agreement between the results of our code and those of the control codes indicates that the populations of the levels involved in the calculations are well determined under LTE or out of LTE, and the methodology followed to resolve the radiation transfer equation is properly implemented and works for a variety of situations, including the modelling of emission from systems displaying maser emission. Thus, our code is expected to give accurate results also in more complex 1D scenarios.

A3.2 2D problem

In this section, we show that our code is capable of dealing with abundances and excitation temperatures depending on r and the polar angle, θ.

Fig. A3 shows the emission of a test line (see Section A3.1) coming from an expanding envelope ($v_{exp} = 5$ km s^{-1}, $n_{H_2} \propto r^{-2}$, thermal line width, optically thin regime) with zero abundance except in two hollow truncated right circular cones with their axes
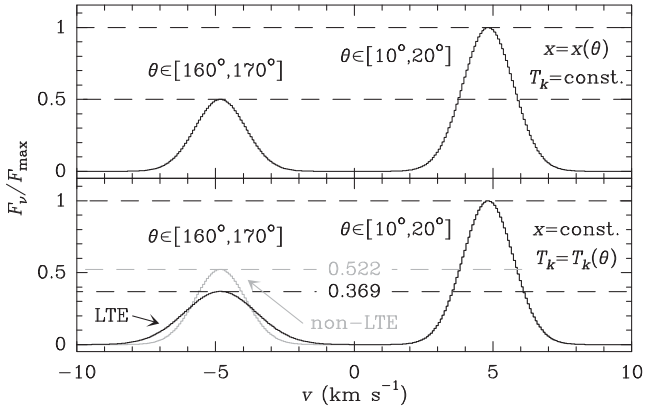
Figure A3. Test line normalized to its maximum from a cloud composed of two hollow cones placed symmetrically behind ($10° \leq \theta \leq 20°$, back cone) and in front of the star ($160° \leq \theta \leq 170°$, front cone). The gas expansion velocity is set to 5 km s^{-1} and the H$_2$ density profile is $\propto r^{-2}$. The abundance is set to zero out of the cones and between 1 and $7R_\star$ to avoid shadowing effects from the star. The cloud is assumed to be under LTE and it is optically thin. The spectrum in the upper insert is calculated with an abundance of 10^{-7} and 5×10^{-8} in the back and front cones, respectively, and a constant $T_k = 100$ K (LTE). The contribution of the front cone is half of the back cone. The black spectrum in the lower insert results from assuming an abundance of 10^{-7} in both cones and $T_k = 100$ and 200 K in the back and front cones, both under LTE. The grey spectrum is calculated under LTE in the back cone with $T_k = 100$ K and out of LTE with $T_k = 100$ K and $T_{exc} = 200$ K in the front cone. Theoretically, the ratio of the integrals of the contributions of the front to the back cones should be of $\simeq 0.522$ for both cases. The ratios of the peaks of the contributions are $\simeq 0.369$ and 0.522 for the LTE and non-LTE scenarios, respectively. The differences between the theoretical values stated above and the results calculated with our code are smaller than 0.05 per cent.

aligned with the LoS (back and front cones) where the abundance is non-zero in three different situations:

Scenario 1: the abundance is twice smaller in the front cone than in the back cone, $T_k = 100$ K in both, and the envelope is under LTE. The contribution from the front cone is the same than from the back cone but scaled by a factor of 0.5, as expected. The discrepancies between the theory and the results of our code are 0.04 per cent.

Scenario 2: the abundance of both cones is equal but $T_k = 100$ and 200 K in the back and front cones, respectively. The envelope is under LTE. The ratio of the integrated flux of the front cone to that of the back cone calculated from the results of our code is in very good agreement with the theoretical predictions within an uncertainty of 0.05 per cent.

Scenario 3: the abundance of both cones is equal but the back cone is under LTE with $T_k = 100$ K and the front cone is rotationally out of LTE with $T_k = 100$ K and $T_{exc} = 200$ K for the modelled line. The ratio of the integrated flux of the front cone to that of the back cone calculated from the results of our code agrees with theoretical predictions with an error of 0.05 per cent.

The code can deal with more complex continuous abundance distributions depending on the polar angle. In Fig. A4, we have plotted the emission of the test molecule coming from a static isothermal envelope under LTE (thermal emission; $n_{H_2} \propto r^{-2}$, $T_k = 100$ K, thermal line width $\simeq 2.1$ km s^{-1}) and under LTE but with an excitation temperature for the computed line of -100 K (maser emission). The adopted abundance distributions are proportional to θ/π and
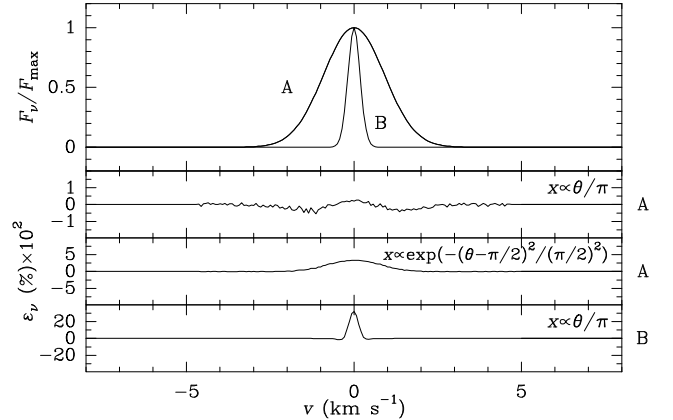

Figure A4. Test line normalized to its maximum from a static isothermal cloud with the abundance $\propto \theta/\pi$ and $e^{-(\theta-\pi/2)^2/(\pi/2)^2}$ (thermal emission, A, and maser emission, B). The H$_2$ density profile is $\propto r^{-2}$. The thermal emission (A) is calculated under LTE with $T_k = 100$ K while the maser emission (B) is computed by assuming $T_k = 100$ K and a $T_{exc} = -100$ K for the test line. In the thermal emission case, the normalized line profile is the same for both abundance distribution. The CMB continuum has been removed. The residuals, ε_ν, are defined as in Fig. A1.

$e^{-(\theta-\pi/2)^2/(\pi/2)^2}$. The emission have been compared to the results of an ad hoc code in which the integral of the optical depth for each impact parameter has been calculated by using the trapezoidal rule. The difference between the results of both codes for the thermal emission is smaller than 0.05 per cent if $\tau_{max} \lesssim 10^4$ and smaller than 0.4 per cent for the maser emission ($\tau_{max} \simeq -17$ with a maximum flux of 9×10^7 Jy).

The good results of these tests reveal that the sampling of the abundance and the temperature distributions are well implemented regarding the polar angle. The populations of the molecular levels are accurately calculated under LTE and out of LTE and the methodology to solve the radiation transfer equation works fine also for an envelope depending on r and θ, regardless of the optical depth of the modelled line.

A3.3 3D problem

In the 3D problem, the physical and chemical magnitudes are allowed to vary with the three spherical coordinates, (r, φ, θ), at the same time.

In Fig. A5, a simple structure to show the performance of the code is plotted. The structure comprises four components (A, B, C and D) that revolve $10°$ in the polar angle around the plane of the sky. The axial angle size depends on the component ($10°$, $30°$, $50°$ and $70°$, respectively). The physical and chemical conditions are the same in every component. The total flux emitted by each component depends linearly on the axial angular size, as expected. This result holds for the optically thick regime since the power to solve the radiation transfer equation showed in the 2D problem (Section A3.2) is inherited in the 3D case. We can compare the flux of the components with that of a continuous ring with the same physical and chemical conditions than the components treated as a 2D problem by scaling the flux of the ring with the ratio of the sizes. The agreement is better than 0.5 per cent.

The ability of the code to define 3D structures depending on the coordinates (r, φ, θ) and to calculate the populations of the
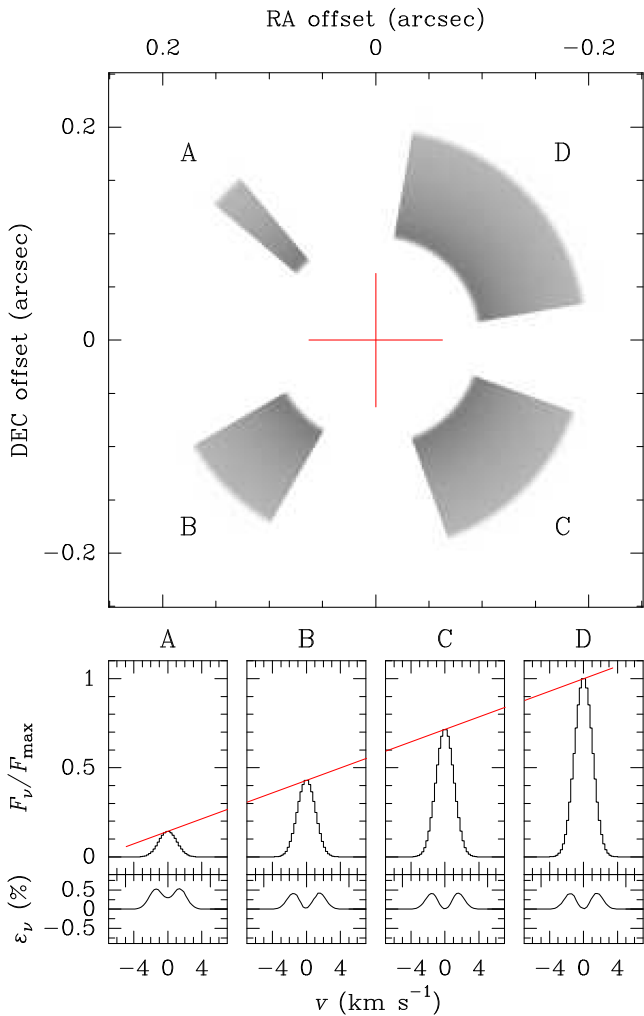
Figure A5. Unconvolved moment 0 map of the emission of the test line showing a structure in the plane of the sky (upper insert). The components of the structure, labelled A, B, C and D, are defined in the ranges of the axial angle [40°, 50°], [120°, 150°], [200°, 250°] and [280°, 350°]. The polar angle varies between 80° and 100° for the whole structure. The distance to the star ranges from 5 to $10R_\star$. The abundance in the rest of the envelope is zero. The H_2 density profile is $\propto r^{-2}$. The kinetic temperature is 100 K and the envelope is under LTE. The gas expansion velocity is 5 km s^{-1}. The emission is optically thin with $\tau \lesssim 0.4$. The spectra of the components of the structure are plotted in the lower inserts. The red line shows that the ratio of the flux of the lines linearly depends, as expected, on the axial angular size of the components. The uncertainty, ε_v, is derived by comparing the spectrum of each component with the scaled spectrum produced by a complete ring with the same conditions (2D problem).

molecular levels and to solve the radiation transfer equation along 2D structures with coordinates (r, θ) makes our code suitable to accurately reproduce the 3D emission of any molecule regardless of the physical and chemical conditions of the emitting cloud.

This paper has been typeset from a TEX/LATEX file prepared by the author.